

# Northumbria Research Link

Citation: Gonzalez Sanchez, Sergio, Pérez, Pablo, Garcés, Gerardo and Adeva, Paloma (2016) Influence of the processing route on the mechanical properties at high temperatures of Mg-Ni-Y-RE alloys containing LPSO-phases. *Materials Science and Engineering: A*, 673. pp. 266-279. ISSN 0921-5093

Published by: Elsevier

URL: <http://dx.doi.org/10.1016/j.msea.2016.07.077>  
<<http://dx.doi.org/10.1016/j.msea.2016.07.077>>

This version was downloaded from Northumbria Research Link:  
<http://nrl.northumbria.ac.uk/27444/>

Northumbria University has developed Northumbria Research Link (NRL) to enable users to access the University's research output. Copyright © and moral rights for items on NRL are retained by the individual author(s) and/or other copyright owners. Single copies of full items can be reproduced, displayed or performed, and given to third parties in any format or medium for personal research or study, educational, or not-for-profit purposes without prior permission or charge, provided the authors, title and full bibliographic details are given, as well as a hyperlink and/or URL to the original metadata page. The content must not be changed in any way. Full items must not be sold commercially in any format or medium without formal permission of the copyright holder. The full policy is available online: <http://nrl.northumbria.ac.uk/policies.html>

This document may differ from the final, published version of the research and has been made available online in accordance with publisher policies. To read and/or cite from the published version of the research, please visit the publisher's website (a subscription may be required.)

[www.northumbria.ac.uk/nrl](http://www.northumbria.ac.uk/nrl)



## Influence of the processing route on the mechanical properties at high temperatures of Mg-Ni-Y-RE alloys containing LPSO-phases

S. González<sup>1</sup>, P. Pérez<sup>2\*</sup>, G. Garcés<sup>2</sup>, P. Adeva<sup>2</sup>

1. Faculty of Engineering and Environment, Northumbria University, Newcastle upon Tyne NE1 8ST, United Kingdom

2 Departamento de Metalurgia Física, Centro Nacional de Investigaciones Metalúrgicas (CENIM-CSIC), Avda. Gregorio del Amo 8, 28040 Madrid, Spain

### Abstract

The mechanical properties at high temperatures of two Mg-Ni-Y-RE alloys prepared by conventional or powder metallurgy routes have been evaluated. All alloys exhibit high-strength up to 250°C but their strength depends more on the composition of the alloy rather than on the processing route. High strength of the alloys arises from their fine grain size but there is an additional contribution of load transfer from the magnesium matrix towards the second phases in the alloys processed by the conventional route while additional hardening in the alloys prepared by powder metallurgy is due to Orowan mechanism. Above 250°C, the strength drops to very low values but all alloys exhibit high elongations and grain boundary sliding is the controlling mechanism. Grain boundary sliding also induces cracking of the coarse second phases into smaller pieces during the initial stages of plastic deformation of conventionally processed alloys.

Keywords: A. Mechanical characterization; B. Magnesium alloys; B. LPSO-phase, C. Processing route; D. Deformation mechanisms.

### 1. Introduction

The mechanical properties of magnesium alloys can be substantially improved by the addition of proper alloying elements [1-4]. Simultaneous addition of transition metal (TM) and rare earth (RE) elements has been proved to harden considerably magnesium, attaining the maximum strengthening when the alloys are reinforced by long period stacking ordered structures (usually

---

\*corresponding autor: Tel.: +34915538900; fax: +34-915347425  
E-mail address: [zubiaur@cenim.csic.es](mailto:zubiaur@cenim.csic.es) (P. Pérez)

named as LPSO-phases) [5-16]. Most of the work has been focused in Mg-Zn-(Y,RE) alloys [10-20], although new Mg-Ni-(Y,RE) alloys have been developed more recently [7,21-24]. Difference among Ni-containing and Zn-containing alloys results from nickel insolubility in the magnesium lattice while zinc exhibits certain solubility. Nickel excess appears in Mg-Ni-Y alloys containing the LPSO-phase as  $Mg_2Ni$  [21,22,25] while zinc can form binary and ternary intermetallic Mg-Zn compounds and/or remain in solid solution within the magnesium lattice [16,18,26,27].

The addition of insoluble rare earth elements such as lanthanum or cerium to ternary alloys results in formation of intermetallic Mg-RE compounds [14,16,17,23]. Due to high atomic Mg/RE ratio in intermetallic Mg-RE phases, small additions of RE elements leads to significant volume fractions of these phases in Mg-Ni-Y-RE alloys [23]. Hardening effect of Mg-RE phases has been reported to be smaller than that associated with LPSO-phases [16,18]. Major effect of Mg-RE phases, however, is to increase the ability of the alloy to deform superplastically [21].

Although the microstructure of Mg-Ni-Y-CeMM alloys processed by a conventional route of extrusion of as-cast rods is fine (the grain size oscillates between 2 and 5  $\mu m$ ), additional refinement could be achieved by using powder metallurgy techniques. The processing route determines the mechanism controlling the deformation at room temperatures, which is associated with the size and distribution of second phases [28]. This effect could be also expected at higher temperatures. Thus, the aim of this research has been to identify the mechanisms controlling the deformation in the temperature range 100-400°C of two Mg-Ni-Y-CeMM alloys prepared through two different processing routes.

## 2. Material and Methods

Two alloys of nominal compositions, given in atomic percentage,  $Mg_{96}Ni_2Y_1CeMM_1$  (designated as MgNi2 alloy) and  $Mg_{94}Ni_3Y_1CeMM_1$  (designated as MgNi3) were obtained from eutectic binary Mg-Y, Mg-RE and Mg-Ni master alloys, adjusting the composition with minor amounts of the pure elements (Mg, Ni, Y) and Ce-rich mischmetal (53 wt. % Ce, 26 wt. % La, 16 wt. % Nd, 5 wt. % Pr). The alloys were casted in bars of 42 mm in diameter. Some of the bars were machined up to 40 mm and hot extruded at 400°C using an

extrusion ratio of 18:1. These materials will be designated as CP (conventional processing)

The remaining bars were remelted to produce rapidly solidified powders (<100  $\mu\text{m}$ ) through the Electrode Induction-Melting Gas Atomization technique. The powders were isostatically cold pressed and then extruded at 400°C using an extrusion ratio of 18:1. These materials will be designated as PM (powder metallurgy)

The microstructure of CP and PM alloys was characterized by optical microscopy (OM) and scanning and transmission electron microscopy (SEM and TEM, respectively), while the identification of the phases was performed by X-ray diffraction (XRD) and EDX microanalysis. A complete microstructural characterization of the alloys can be found elsewhere in reference 24.

Tensile mechanical properties were evaluated in the temperature range 100-400°C. Cylindrical samples of 3 mm radius and 10 mm gauge length were machined from the extruded bar with their longer dimension parallel to the extrusion direction. Tensile tests were performed at an initial strain rate of  $10^{-4} \text{ s}^{-1}$  in a universal Instron tensile machine. The stress exponent was determined through jump strain rate tests. In these tests, the specimens were initially deformed at a strain rate of  $10^{-4} \text{ s}^{-1}$  until a steady state was reached. The strain rate was then reduced to  $10^{-5} \text{ s}^{-1}$  until a new steady state was again attained. Successive changes in the strain rate were carried out following this procedure.

### 3. Results

The microstructure of the extruded alloys is presented in Fig. 1. The microstructure consists of a fine-grained magnesium matrix embedding a high volume fraction of second phases. Second phases are coarse and arranged in strings along the extrusion direction in CP alloys while they are equiaxed and much finer in PM alloys. The grain size was fine for all alloys, especially for both PM alloys. It was 4  $\mu\text{m}$  for CP-MgNi<sub>2</sub>, 2  $\mu\text{m}$  for CP-MgNi<sub>3</sub> and 0.5  $\mu\text{m}$  for the PM alloys. The volume fraction of second phases was 27 and 52 % for the MgNi<sub>2</sub> and MgNi<sub>3</sub> alloys, respectively. To get a more complete description of the microstructure of all alloys, the readers are referred to a previous work [28]

True-stress-true strain curves between 100 and 400°C at  $10^{-4} \text{ s}^{-1}$  are presented in Fig. 2 for all materials while the evolutions of yield stress, maximum strength and elongation to failure with the test temperature are presented in Fig. 3. According to the data, two different behaviours can be clearly distinguished depending on the temperature, with a transition at about 250°C: (a) At low temperatures, below 250°C, all the alloys exhibit high yield stresses. (b) Above 250°C, however, the yield stress drops to very low values. This significant decrease in strength is accompanied by a considerable increase in the elongation to failure, especially in the case of CP alloys.

### 3.1 Low temperature interval (100-200°C)

At 100 and 200°C, the maximum strength always corresponds to the high-alloyed material (MgNi<sub>3</sub> alloy), although the differences tend to decrease gradually with increasing the test temperature. Furthermore, for a given composition, the alloy processed by powder metallurgy always attains the maximum strength. At 100°C, the yield stress oscillates between the 402 MPa for the PM-MgNi<sub>3</sub> alloy and the 220 MPa for the CP-MgNi<sub>2</sub> alloy. The ductility of both MgNi<sub>3</sub> alloys is very low, not higher than 2 %. On the contrary, CP-MgNi<sub>2</sub> and PM-MgNi<sub>2</sub> combine high strength with some ductility. Furthermore, elongation to failure of the PM-MgNi<sub>2</sub> alloy was almost twice that of CP-MgNi<sub>2</sub> alloy (21 % against 11 %). The different ductility among CP-MgNi<sub>2</sub> and PM MgNi<sub>2</sub> alloys, also found at room temperature [28], results from the different deformation mechanism operating in each alloy. The fine equiaxed microstructure of PM MgNi<sub>2</sub> alloy promotes the stress is uniformly supported by all the grains. Stress distribution is more heterogeneous in the case of CP-MgNi<sub>2</sub> alloy because magnesium grains transfer load into the coarse second phases. When second phase cracks, the load comes back to the magnesium grain and, if the stress is not supported by the magnesium grains or by other second phases, nucleation and propagation of the crack proceeds catastrophically. As this behaviour was also reported at room temperature [28], it can be concluded that the use of the powder metallurgy route induces not only a benefit on the strength but also on the ductility of the MgNi<sub>2</sub> alloy while the second phases can harden the PM alloy.

At 200°C, the highest yield stress is found for the PM-MgNi<sub>3</sub> (270 MPa), but the maximum strength corresponds to the CP-MgNi<sub>3</sub> (335 MPa) because of its greater hardening during plastic regime. Precisely, the absence of hardening in PM alloys during plastic deformation at 200°C is the most noticeable difference with CP alloys. Unlike at 100°C, the ductility is practically the same for CP-MgNi<sub>2</sub> and PM MgNi<sub>2</sub> alloys. Continuous load transfer from the magnesium matrix induces continuous hardening during plastic flow (see tensile curves of Fig. 2b) which promotes large elongations than that found at 100°C. On the other hand, the fine precipitates of the PM-MgNi<sub>2</sub> alloy are not effective obstacles for dislocation motion, favouring premature failing of the material with elongations around 21 %, very close to the value found at 100°C.

It is interesting to note the presence in the true stress-true strain curves of a yielding phenomenon restricted exclusively to the MgNi<sub>2</sub> alloy at 100 and 200°C. At 100°C, the stress for the PM-MgNi<sub>2</sub> alloy remains almost stable up to 3 % of strain and, then, the hardening stage commences. In the case of the CP-MgNi<sub>2</sub> alloy, the yield point is followed by a slight decrease in the stress, immediately followed by the hardening stage. At 200°C, both MgNi<sub>2</sub> alloys exhibit also the yield point phenomenon but hardening takes place in CP-MgNi<sub>2</sub> alloy while a steady state is attained in the PM-MgNi<sub>2</sub> alloy once the upper yield point is surpassed. The occurrence of yield point phenomenon in magnesium alloys is usually associated with the segregation of tiny particles within the magnesium grains [29-31]. These particles pin down or anchor dislocations, causing an increase in the stress up to a critical value is attained (upper yield stress). Once the upper yield point is reached, there is a load drop due to unpinning of dislocations which is more noticeable in the PM alloy because of the higher volume fraction of fine precipitates inside the magnesium grains. Probably, the absence of yield point phenomenon in tensile curves of MgNi<sub>3</sub> alloys is due to the low volume fraction of the magnesium phase (only 48 %) which can dilute or mask the occurrence of such process in tensile curves.

### *3.2 Transition temperature (250°C)*

Transition from the high-strength behaviour at low temperatures to that of low strength at high temperatures is noticed at 250°C. Compared to 200°C, the yield stress experiences a significant decrease although it still remains relatively high.

Nevertheless, the degree of the decrease is minimised in the case of conventionally processed alloys. Thus, for instance, the yield stress decreases about 60 % for PM-MgNi<sub>3</sub> alloy (from 272 MPa at 200°C to 111 MPa at 250°C) against the 32 % for the CP-MgNi<sub>3</sub> alloy (from 256 MPa at 200°C to 175 MPa at 250°C). Elongation to failure of PM alloys, about 100-125%, was almost twice that of CP alloys.

### 3.3 High temperature interval (300-400°C)

The yield stress drops off below 60 MPa independently of the composition of the alloys and the processing route. These values decrease below 5 MPa when the temperature rises up to 400°C (see Fig. 3). All curves show certain hardening in the course of plastic deformation as temperature increases, being more significant for the CP-MgNi<sub>2</sub> alloy. Such hardening arises, probably, from grain coarsening during plastic deformation and it results in a considerable increase in stress. Usually, the maximum stress can be 1.5-3 times higher than the stress in the yield stress.

### 3.4 Calculation of stress exponent

Fig. 4 plots the strain rate-true stress in the steady state in a double logarithmic at different temperatures for all materials between 100 and 400°C according to the general-power law constitutive creep equation

$$\dot{\varepsilon} = K \sigma^n e^{(-Q/RT)}$$

where K is the creep constant, n the apparent stress exponent,  $\sigma$  the stress in the steady state, Q the apparent activation energy, T the absolute temperature and R the universal gas constant. Table 1 lists the values of the stress exponent *n* at different temperatures for all the alloys. At 100°C only data of MgNi<sub>2</sub> alloys are presented because of the low ductility of MgNi<sub>3</sub> alloys. Although a complete steady state is not attained in tensile curves of the CP-MgNi<sub>2</sub> alloy, strain rate jumps were carried out in very short strain intervals (2.5 %) in which no relevant microstructural changes are expected, as confirmed by the excellent correlation among the different points. The stress exponent *n* takes very high values; 22 and 35 for CP-MgNi<sub>2</sub> and PM-MgNi<sub>2</sub> alloy, respectively. At 200°C, the highest *n*

corresponds to CP-MgNi<sub>2</sub> alloy,  $n=46$ , being 29 for the PM-MgNi<sub>2</sub> alloy. It is interesting to remark that  $n$  for both MgNi<sub>3</sub> alloys is significantly lower than for MgNi<sub>2</sub> alloys (16 for CP-MgNi<sub>3</sub> and 18 for PM-MgNi<sub>3</sub>). At 300°C, the value of  $n$  depends on the strain rate. As a general rule,  $n$  takes values around 5-8 at high strain rates, corresponding the lowest values to PM alloys and the highest values to CP alloys. At low strain rates, however,  $n$  is close to 2-3. In addition, new transition towards values higher than 5-6 is observed for the PM alloys at the lowest strain rates. As the temperature increases, all the intervals with different  $n$  are shifted to higher strain rates, as can be checked in Table 2. Moreover, the region in which  $n$  is close to 2 seems to be wider as the temperature increases. For instance,  $n$  is about 2.5 in the  $10^{-5}$ - $10^{-2}$  s<sup>-1</sup> interval at 350°C for CP-MgNi<sub>3</sub> material.

The activation energy of the process was determined in the superplastic regime,  $n$  close to 2-2.5, plotting in a double logarithmic manner the  $\sigma/E$  against the inverse of the absolute temperature. For CP alloys, the activation energy is 181 kJ/mol (at stress of 20 MPa) and 214 kJ/mol (at stress of 30 MPa) for CP-MgNi<sub>2</sub> and CP-MgNi<sub>3</sub> alloys, respectively. In the case of PM materials, the values are 208 kJ/mol (at stress of 44 MPa) and 294 kJ/mol (at stress of 38 MPa) for PM-MgNi<sub>2</sub> and PM-MgNi<sub>3</sub> alloys, respectively. These energies are much higher than the activation energy for grain boundary (92 kJ/mol) or lattice diffusion (135 kJ/mol) in magnesium [32,33], but they are not so far from the activation energies for LPSO-containing magnesium alloys which range between 182 and 276 kJ/mol [17,34-36]. This suggests that activation energy for alloys containing high volume fractions of LPSO-phases is higher than for diluted magnesium alloys. This indicates that interfaces or LPSO-phase itself could play a significant role during the superplastic regime of the alloys.

### 3.5 Microstructure of deformed samples

Microstructural examination of the deformed samples has been carried out in the three intervals in which the mechanical behaviour has been divided. The observations evidence differences in the mechanism controlling plastic deformation of CP and PM alloys, independently of the composition of the alloy. This clearly confirms that the processing route determines markedly the deformation behaviour of Mg-Ni-Y-CeMM alloys rather than their composition.



Fig. 5 shows the microstructure in two regions of a CP-MgNi<sub>2</sub> sample tested at 200°C at 10<sup>-4</sup> s<sup>-1</sup>. The microstructure in Fig. 5a resembles that of the non-deformed alloy and corresponds to the region outside the necked region. On the other hand, Fig. 5b shows the microstructure in the necked area. Here, two main changes occur in the microstructure of the alloy: Firstly, second-phase particles, especially Mg<sub>17</sub>RE<sub>2</sub> particles, are fragmented. Secondly, magnesium grains are elongated along the tensile direction. In the case of PM alloys, some cavities were developed in the course of the deformation in the region close to the fracture, as shown in Fig. 6a. Most of second phase particles remain intact outside the necked region (see Fig. 6b) but the number of cracked particles increases progressively towards the fracture surface, within the necked region, as shown in Fig. 6c. Etched samples demonstrate that initially equiaxed grains are elongated along the tensile direction, especially those grains close to the fracture region, as shown in Fig. 7a-c.

At the transient temperature of 250°C, no significant changes are noticed with respect to samples deformed at 200°C. Major difference is that cracking of Mg<sub>17</sub>RE<sub>2</sub> particles occurs from the earliest stages of plastic deformation over the entire gauge length, although the amount of fragmented particles is lessened outside the necked area (see Fig. 8). Etched samples reveal magnesium grains severely deformed along the tensile direction within the necked region, especially those grains close to the fracture surface (see insets of Fig 8). In the case of PM alloys, small cavities were observed, mainly concentrated in the region close to the fracture. The tendency for cavity development is higher in the PM-MgNi<sub>3</sub> alloy, as can be seen in Fig. 9. Etched samples proved that magnesium grains are deformed for the PM-MgNi<sub>2</sub> alloy and hardly deformed for the PM-MgNi<sub>3</sub> alloy (Fig. 10).

Microstructural evolution during the tensile test is completely different for the alloys deformed above 250 °C. In the case of CP alloys, considerable refinement of second phases takes place from the initial stages of deformation, as shown in Fig. 11 for the CP-MgNi<sub>3</sub> alloy. Moreover, the small fragments resulting from the cracking of second phases are redistributed homogeneously throughout the magnesium matrix in such a way that the arrangements of second phases, initially existing as strings perfectly orientated along the extrusion direction, disappear in the course of plastic deformation (see Fig. 12).

In addition, magnesium grains retain their equiaxed shape and only at the highest test temperature of 400°C some grain coarsening is noticed, although grain growth is hampered in the deformed region when compared with grain size in the non-deformed heads of tensile samples. At 300°C some cavities are found in the deformed region, but the tendency to form cavities decreases with increasing the test temperature. For instance, no cavities are found in the sample deformed 250 % at 400°C. Another significant change in the microstructure is recrystallization of coarse-grained areas during straining. At 300°C recrystallization is partial but it is total at 400°C (see Fig. 12). In the case of PM alloys, the most noticeable feature found in samples tested at temperatures higher than 250°C is the high propensity to cavitation, especially for the PM-MgNi<sub>2</sub> alloy, as observed in Fig. 13. Cavities are usually concentrated in the necked region, especially close to the fracture surface. They are arranged as long strings, up to 30 μm in length and 2 μm in width, aligned along the tensile direction. Occasionally, these strings can coalesce, originating cavities up to 20 μm width. The size and number of cavities decrease progressively as moving away from the fracture surface, adopting the appearance of fine porosity far away from the fracture region.

#### 4. Discussion

The results of this study reveal that high-strength of Mg-Ni-Y-CeMM alloys can be retained up to 250-350 MPa at 200°C and around 175-250 MPa at 250°C. These values are much higher than those reported for commercial magnesium alloys such as alloys belonging to AZ, AM, AS, ZK or ZE families in which the strength falls down to very low values when the temperature exceeds 100-150°C [3]. Furthermore, the maximum strength is higher than those of commercial alloys such as WE43 or WE54 which are designed for applications up to 200°C, with the advantage that the maximum strength is achieved without long ageing treatments. The same behaviour is found in the same alloys when they are processed by extrusion of rapidly solidified ribbons [37]. In this case, the maximum strength can attain about 500 MPa at room temperature, although these values decrease rapidly above 100-150°C, even in the case of WE43 or WE54 alloys.

Tensile tests evidence how the composition and the processing route determine the mechanical strength of Mg-Ni-Y-CeMM alloys between 100 and 400°C. The intervals agree rather well with the two different behaviours identified through tensile testing. At temperatures up to 200°C, the strength depends more on the composition of the alloy than in the processing route, as found at room temperature [28]. The strength of MgNi3 alloys is higher than for MgNi2 alloys because of the higher volume fraction of hard second phases. The effect of alloy composition in the mechanical properties, however, becomes irrelevant beyond 200°C because above this temperature the higher strengths correspond to CP alloys.

The microstructure among the alloys prepared following the same processing route is very similar, varying only the volume fraction of second phases (about 27 % for the MgNi2 alloy and about 52 % for the MgNi3 [28]). Major differences between CP and PM alloys are:

- (1) Type of the second phases. Common phases for the alloys processed by both routes are Mg, intermetallic Mg-RE phases, Mg<sub>2</sub>Ni and LPSO-phase while fine Mg<sub>24</sub>Y<sub>5</sub> precipitates are exclusively present in both PM alloys.
- (2) Shape, size and morphology of the phases. Second phases in PM alloys are finer and more equiaxed than in CP alloys.
- (3) Their distribution in the magnesium matrix. Second phases are homogeneously distributed in the magnesium matrix in PM alloys while they are concentrated in bands as strings of coarse particles arranged along the extrusion direction in the case of CP alloys.
- (4) Grain size of the magnesium matrix. Around 0.5 μm for PM alloys and smaller than 4 μm for CP alloys (2 and 4 μm for CP-MgNi3 and CP-Mg-Ni2 alloys, respectively). It is interesting to note that there are coarse non-recrystallised areas in CP alloys, especially in the case of the CP-MgNi3 alloy.
- (5) Size and morphology of the LPSO-phase. LPSO-phase appears as long blocks, up to 20-30 μm in length, oriented in the extrusion direction in CP alloys while it appears as long lamella up to 500 nm length and 1 nm thick within the magnesium grains in PM alloys.

These microstructural differences should account for the different mechanical behaviour found between CP and PM alloys.

At 100°C and 200°C, the maximum strength corresponds to MgNi<sub>3</sub> alloys, as also found at room temperature [28]. The main strengthening effect is related to the fine grain size of the alloys and the higher volume fraction of second-phase particles, 52 % in MgNi<sub>3</sub> alloys compared to 27 % in MgNi<sub>2</sub> alloys. For CP alloys hardening is mainly attributed to high contribution of Hall-Petch mechanism due to the fine grain size of the alloys but load transfer from the magnesium matrix to the coarse second phases also has a significant contribution because Young moduli of Mg-RE compounds [39] and LPSO phase [39-41] is higher than that of the magnesium matrix. For PM alloys, contribution of grain boundary strengthening is still higher because of the fine-grained magnesium matrix (around 0.5 μm) although the reinforcing due to the multiple phases existing in PM alloys can be also relevant through other two mechanisms: (i). Composite strengthening, due to load transfer from the magnesium matrix towards second-phase particles of about 0.5 μm in size homogeneously dispersed in the magnesium matrix, is manifested by the presence of isolated second phase particles broken in the deformed samples, as seen in Fig. 6c. (ii) Hardening induced through Orowan mechanism by dislocations interacting with thin LPSO-phase plates and fine Mg<sub>24</sub>Y<sub>5</sub> precipitates inside the magnesium grains.

All alloys show high  $n$  values at 100 and 200°C, always above 15, indicative that the deformation is controlled by dislocation motion. Such high values are generally attributed to the existence of a threshold stress. It is interesting to note that  $n$  values are much higher than those reported for PM magnesium alloys [42-45] or magnesium composites [46-48], with a maximum value of 19 at 200°C for strongly textured PM Mg [44]. This indicates that high  $n$  values in Mg-Ni-Y-CeMM alloys are associated with the second phases present in the alloy rather than with the fine oxide dispersion existing in PM alloys [43]. Moreover,  $n$  depends not only on the processing route but also on the temperature and alloy composition. At 100°C  $n$  is much higher for PM-MgNi<sub>2</sub> alloy than for the CP MgNi<sub>2</sub> alloy, 35 against 22. This indicates that dislocation motion is more hindered in the PM alloy than in the CP alloy. This difference in the  $n$  value should result from large contribution of a mechanism operating in the PM alloy

that hardly contributes in the CP alloy. This mechanism should correspond to hardening induced by the fine second phases inside the magnesium grains (Orowan strengthening). Orowan hardening is significant up to 100°C because the distance between precipitates inside the magnesium grains is small [28], resulting in a strain hardening during the plastic flow of the PM-MgNi<sub>2</sub> alloy comparable to that found in the CP-MgNi<sub>2</sub> alloy. At 200°C, however, Orowan hardening becomes less effective because dislocations can overpass more easily these obstacles by temperature assisted mechanisms such as dislocation glide or dislocation climb, so this mechanism does not induce hardening during the plastic flow. Nevertheless, the contribution of load transfer mechanism becomes higher, as noticed from a higher amount of broken second-phase particles and the constant strain hardening observed in the course of plastic deformation at 200°C. The subsequent balance results in a decrease in  $n$  from 35 at 100 °C to 29 at 200°C. Such effect is also reflected in the strain hardening of the samples tested at 100 and 200°C. Similar behaviour is found for the PM-MgNi<sub>3</sub> alloy, although the material tested at 200°C still shows a slight hardening during plastic deformation due to the smaller volume fraction of the magnesium phase reduces the contribution of Orowan and load transfer mechanisms to the total strength of the alloy compared to that in the PM-MgNi<sub>2</sub> alloy. This accounts for the lower  $n$  calculated for the PM-MgNi<sub>3</sub> alloy compared to the PM-MgNi<sub>2</sub> alloy, 16 and 29 respectively at 200°C.

On the other hand,  $n$  for the CP-MgNi<sub>2</sub> alloy shifts from 22 at 100°C to 46 at 200°C. That is, the strain rate sensitivity of the alloy is greatly decreased as the temperature is increased within this temperature interval. This implies that dislocation motion is significantly hindered at 200°C. Such high  $n$  values can be explained considering load transfer from magnesium grains to coarse second phases (almost equiaxed Mg<sub>17</sub>RE<sub>2</sub> and elongated LPSO-phases blocks) as the main mechanism controlling plastic deformation. If the alloys are considered as a composite, the ratio of the strain rates of the composite and the metallic matrix is given by  $(1-\alpha)^n$ , where  $\alpha$  is the load-transfer coefficient ranging from 0 (no load transfer) to 1 (full load transfer) and  $n$  is the stress exponent [48-52]. Apparently, not significant changes in  $n$  values could be expected if the load transfer mechanism is the same at low temperatures. Nevertheless, the mechanical behaviour of the phases evolves in different ways with increasing

the temperature; (i) Magnesium softening due to critical resolved shear stress of main slip systems in magnesium drops to very low values above 150°C [53]. Consequently, the stress transferred by the magnesium grains towards the second phases becomes proportionally higher as the test temperature increases, (ii) The high strength of the LPSO-phase is retained but its ductility increases gradually up to 200°C [54,55] and (iii) hardness of Mg-RE compound is the highest among the phases existing in the alloy [16,18] but its ordered structure renders this phase inherently brittle. Major brittleness of the Mg-RE phase has been reported for Mg-Zn-Y-RE alloys with different Y/RE ratios [18]. The strength and ductility of these alloys were improved as increases the Y/RE ratio, i.e. as the volume fraction of the LPSO-phase prevails over that of Mg-RE phase. At low temperatures, both Mg-RE and LPSO-phase are brittle but the fine-grained magnesium matrix is also very hard in such a way that the failure takes place when the additional stress supported by the second phases is not much higher than the applied stress. This is confirmed by the absence of cracking in any kind of particle outside the fracture surface [28]. On the other hand, observation of deformed samples only reveals multiple cracking of Mg-RE particles, even out of necking region but not of the LPSO-phase. This means that intermetallic Mg-RE particles cannot bear the load transferred by the magnesium matrix. Moreover, the stress released when these particles are broken must be re-transferred towards the LPSO-phase because this phase combines high yield strength as well as high ductility and considerable strain hardening in the course of plastic deformation within this temperature interval [54,55]. This different behaviour of Mg-RE and LPSO-phase particles with the temperature changes the load transfer contribution of each phase. The stress transferred below 200°C is low and it can be assumed by both Mg-RE and LPSO-phase particles until cracking of these phases takes place, resulting in lower  $n$  values. At high temperatures, magnesium matrix may transfer a significant part of the stress which is mainly supported by the LPSO-phase, leading to high  $n$  values.

It is interesting to note that  $n$  at 200°C is much higher for the CP-MgNi<sub>2</sub> alloy than for the CP-MgNi<sub>3</sub> alloy (46 against 18), so load transfer should be more effective in the former alloy. The lower volume fraction of magnesium phase in the CP-MgNi<sub>3</sub> alloy implies a reduction in the load transfer contribution to

strengthen the alloy. Furthermore, second-phase particles not in direct contact with magnesium grains will not aid in load transfer. This means that load transfer in CP-MgNi<sub>2</sub> alloy could be enlarged due to a more homogeneous distribution of the second phases which maximizes the number of magnesium grains transferring stress to second-phase particles.

Above 250°C, the strength of all alloys falls down to very low values. In addition,  $n$  values decrease up to 2-8 depending on the material, temperature and strain rate interval. At all temperatures,  $n$  values around 2-3 can be found within a certain strain rate range in which the alloys exhibit high elongations to failure, (up to 720 % for the CP-MgNi<sub>2</sub> alloy deformed at 350°C at  $10^{-4} \text{ s}^{-1}$ , as shown in Fig. 3c). The relatively equiaxed shape of magnesium grains after the deformation, the low stress at which plastic flow progresses and  $n$  values close to 2, suggest the deformation under these conditions is controlled by grain boundary sliding (GBS). Nevertheless, the mechanism proceeds in different ways in CP and PM alloys. The deformation mechanism in CP alloys is very complex due to concomitant mechanisms can operate in the course of plastic deformation [17,56]. The initial microstructure evolves continuously during the plastic deformation. The sequence of microstructural changes is the following [56]: (1) Grain boundary/interface sliding from the initial stages of plastic deformation. The size of second-phase particles is too big to expect mutual sliding during the initial stages of deformation. Nevertheless, a good interface, free of defects, permits the sliding of magnesium grains along the long interfaces with the second phases existing in the alloy, i.e. Mg-RE/Mg and LPSO-phase/Mg interfaces, without cavity formation. The role of interfaces in the deformation mechanism is manifested by the high activation energy calculated, higher for the alloy containing a higher volume fraction of second-phases. (2) Cracking of second phase particles. To accommodate sliding without cavity formation, dislocations must be generated at both sides of the sliding interfaces. At the strain rate used for tensile tests,  $10^{-4} \text{ s}^{-1}$ , such dislocations can be easily removed from the interface in the magnesium phase but not in the case of the Mg-RE compounds and LPSO-phase because of their ordered structures. As a consequence, sliding induces dislocations pile-ups in the second-phase particles at the vicinity of the sliding interface, which can result in considerable local stresses accumulation [17]. If a critical stress is

exceeded, cracking of the second-phase particles takes place, as experimentally observed. This mechanism explain LPSO-phase cracking after very short strains at very low applied stresses while such cracking is absent at 250°C at much higher applied stresses. (3) Homogeneous redistribution of second phases in the magnesium matrix. Microstructural observations clearly demonstrate that fragments resulting from multiple fractures of second phases are redistributed into the magnesium matrix. Such redistribution implies certain modification in the mechanism controlling the superplastic flow with respect that occurring during the initial stages. Refinement of large particles into smaller ones would permit the rotation of magnesium grains during grain boundary sliding [57,58]. This mechanism should permit the gradual displacement of second-phase pieces inside the magnesium bands, initially free of them. Cracking of the second phases predominates during the initial stages and becomes less important as the deformation proceeds. This accounts for the limited particle redistribution found after high elongations, as shown in Fig. 14. The microstructure of the samples deformed at 300°C up to 110 % resembles rather well the initial microstructure, although the refinement of second phases is noteworthy. On the contrary, grain rotation is favoured as the size of second-phase fragments is reduced. Once this mechanism becomes predominant, the distribution of the small second-phase particles occurs quickly, as deduced from comparison of the sample deformed 120 and 250 %. (see Fig. 14). (4) Recrystallization of non-recrystallised regions. It is well known that a fine-grained structure is a requisite for the occurrence of GBS. Non-recrystallised areas could constitute an obstacle for GBS/grain rotation.

The extremely large elongations of CP-MgNi<sub>2</sub>, almost two times that of CP-MgNi<sub>3</sub> alloy, is due to the optimal volume fraction of second phases. The volume fraction of second phases is 27 % for CP-MgNi<sub>2</sub> and 52 % for CP-MgNi<sub>3</sub>. Microstructural observations reveal the excellent compatibility among the different interfaces for sliding during the initial stages of plastic deformation, leading to fracture of second phases. Then, grain rotation of magnesium grain is accommodated by the cracked second phases, resulting in the gradual redistribution of second phases. Once the second phases become homogeneously dispersed, the particles can hinder/block further grain rotation, being easier when the volume fraction is very high, i.e. in CP3-MgNi alloy.



In the case of PM alloys the mechanism is simpler. As expected from the homogeneity of the fine dispersion of second phases in a fine-grained magnesium matrix (around 0.5  $\mu\text{m}$ ) and the absence of coarse non-recrystallized regions, the conditions for superplasticity should coincide with the last stage of deformation in CP alloys. Since the grain size of the alloy is smaller, an improvement in the superplastic behaviour could be expected for PM alloys compared to CP alloys. In fact, the elongation to failure of both PM alloys at 250°C is already twice that of CP alloys. Even, at 300°C, the maximum elongation of all materials corresponds to the PM-MgNi<sub>2</sub> alloy (around 400%). At higher temperatures, however, the elongation tends to decrease gradually in such a way that both PM alloys do not behave superplastically. The microstructure after deformation is identical to that of non-deformed samples, and just some grain coarsening up to sizes about 1-1.5  $\mu\text{m}$  is observed at 350 and 400°C. According to  $\dot{\epsilon}$ - $\sigma$  plots the superplastic range, with  $n \approx 2$ , is shifted to higher strain rates than in the case of CP alloys. At 300°C, the interval in which  $n \approx 2.5$  is comprised between  $10^{-4}$  to  $10^{-2}$   $\text{s}^{-1}$ , and at 350°C and 400°C  $n \approx 2$  at strain rates higher than  $10^{-3}$  and  $10^{-2}$   $\text{s}^{-1}$ , respectively. Consequently, both PM alloys are outside the superplastic regime when tested at  $10^{-4}$   $\text{s}^{-1}$  at 350 and 400°C. An increase in the strain rate should be enough to attain superplastic conditions. The tendency of PM alloys to develop cavities is an indication of inadequate accommodation of the dislocations in regions where grain rotation is occurring. It is interesting to note that the number of cavities as well as their size are higher for the PM-MgNi<sub>2</sub> alloy than for PM-MgNi<sub>3</sub> alloy. This suggests that deformation in the PM-MgNi<sub>2</sub> alloy can proceed with a higher volume fraction of cavities while a lower volume fraction of them leads to premature failure in the PM-MgNi<sub>3</sub> alloy. This implies that elongation depends on the volume fraction of second phases. An optimal volume fraction of second phases is required to accommodate rotation of grains as well to restrict grain coarsening in the course of superplastic flow. A higher volume fraction could make harder grain rotation, preventing further rotation or even favouring cavity formation.

## 5. Conclusions

From this research, the following conclusions can be drawn:

1. Below 200°C, the highest yield stress values correspond to the alloys with higher nickel contents. This is indicative that the yield stress depends more on the composition of the alloy than in the processing route, although for a given composition the maximum value is achieved in PM alloys.
2. Mechanical strength of CP alloys is due to the combined effect of fine grain size and significant load transfer from the magnesium grains towards the hard second phase particles. Inferior grade of aggregation in second-phase arrangements of the MgNi<sub>2</sub> alloy compared to the MgNi<sub>3</sub> alloy favours a more effective load transfer.
3. The mechanical strength of PM alloys is due to their fine grain size, smaller than 1 μm, and the hardening effect of very fine second phase particles.
4. Independently of the composition and/or the processing route followed to prepare the alloys, the strength of the alloys above 200°C drops to very low values although they exhibit superplastic behaviour.
5. Superplasticity of CP alloys proceeds through a complex mechanism involving grain boundary/interface sliding from the initial stages of plastic deformation, recrystallization of coarse-grained areas, multiple cracking of coarse second phases and their subsequent redistribution in the magnesium matrix. The deformation mechanism of PM alloys is simpler and it coincides with the last stage of deformation in CP alloys.

### Acknowledgements

We would like to acknowledge financial support of the Spanish Ministry of Economy and Competitiveness (MINECO) under project number MAT2012-34135. We would like to acknowledge the support of Alfonso Garcia Delgado of the CENIM Microscopy Unit for assistance with electron microscopy studies.

### References

- [1] A Luo, M.O. Pekguleryuz, Cast magnesium alloys for elevated temperature applications, *J. Mater. Sci.* 29 (1994) 5259–5271.
- [2] I.J. Polmear, *Light Alloys*, 3rd ed. Arnold, London (1995).
- [3] M.M. Avedesian, H. Baker (Eds.), *Magnesium and Magnesium Alloys*, ASM International (1999).

- [4] A.A. Luo, Recent magnesium alloy development for elevated temperature applications, *Int. Mater. Rev.* 49 (2004) 13–30. doi: 10.1179/095066004225010497.
- [5] M. Jiang, X. Su, H. Li, Y. Ren, G. Qin, The phase equilibria and thermal stability of the long-period stacking ordered phase in the Mg–Cu–Y system, *J. Alloys Compd.* 593 (2014) 141–147. doi:10.1016/j.jallcom.2014.01.042.
- [6] G. Garcés, P. Pérez, S. González, P. Adeva, Development of long-period ordered structures during crystallisation of amorphous  $Mg_{80}Cu_{10}Y_{10}$  and  $Mg_{83}Ni_9Y_8$ , *Int. J. Mater. Res. (formerly Z. Metallkd.)* 97 (2006) 404–408. doi: 10.3139/146.101231.
- [7] T. Itoi, K. Takahashi, H. Moriyama, M. Hirohashi, A high-strength Mg–Ni–Y alloy sheet with a long-period ordered phase prepared by hot-rolling, *Scr. Mater.* 59 (2008) 1155–1158. doi:10.1016/j.scriptamat.2008.08.001.
- [8] Y. Kawamura, T. Kasahara, S. Izumi, M. Yamasaki, Elevated temperature Mg<sub>97</sub>Y<sub>2</sub>Cu<sub>1</sub> alloy with long period ordered structure, *Scr. Mater.* 55 (2006) 453–456. doi:10.1016/j.scriptamat.2006.05.011.
- [9] M. Matsuura, K. Konno, M. Yoshida, M. Nishijima, K. Hiraga, Precipitates with Peculiar Morphology Consisting of a Disk-Shaped Amorphous Core Sandwiched between 14H-Typed Long Period Stacking Order Crystals in a Melt-Quenched Mg<sub>98</sub>Cu<sub>1</sub>Y<sub>1</sub> Alloy, *Mater. Trans.* 47 (2006) 1264–1267. doi:10.2320/matertrans.47.1264.
- [10] J.F. Nie, X. Gao, S.M. Zhu, Enhanced age hardening response and creep resistance of Mg–Gd alloys containing Zn, *Scr. Mater.* 53 (2005) 1049–1053. doi:10.1016/j.scriptamat.2005.07.004.
- [11] G. Garcés, M. A. Muñoz-Morris, D.G. Morris, P. Perez, P. Adeva, Optimization of strength by microstructural refinement of MgY<sub>2</sub>Zn<sub>1</sub> alloy during extrusion and ECAP processing, *Mater. Sci. Eng. A.* 614 (2014) 96–105. doi:10.1016/j.msea.2014.07.012.
- [12] G. Garcés, P. Pérez, S. Cabeza, H.K. Lin, S. Kim, W. Gan, P. Adeva, Reverse tension/compression asymmetry of a Mg–Y–Zn alloys containing LPSO phases, *Mater. Sci. Eng. A.* 647 (2015) 287–293. doi:10.1016/j.msea.2015.09.003.
- [13] Y. Kawamura, K. Hayashi, A. Inoue, T. Masumoto. Rapidly solidified powder metallurgy Mg<sub>97</sub>Zn<sub>1</sub>Y<sub>2</sub> alloys with excellent tensile yield strength above

- 600 MPa, *Mater Trans* 42 (2001) 1172-1176. doi:10.2320/matertrans.42.1172.
- [14] M. Matsuda, S. Ii, Y. Kawamura, Y. Ikuhara, M. Nishida, Variation of long-period stacking order structures in rapidly solidified Mg<sub>97</sub>Zn<sub>1</sub>Y<sub>2</sub> alloy, *Mater. Sci. Eng. A* 393 (2005) 269–274. doi:10.1016/j.msea.2004.10.040.
- [15] G. Garcés, E. Oñorbe, F. Dobes, P. Pérez, J.M. Antoranz, P. Adeva, Effect of microstructure on creep behaviour of cast Mg<sub>97</sub>Y<sub>2</sub>Zn<sub>1</sub> (at.%) alloy, *Mater. Sci. Eng. A* 539 (2012) 48–55. doi:10.1016/j.msea.2012.01.023.
- [16] P. Pérez, G. Garcés, M. Maeso, P. Adeva, Effect of Zn content on microstructure and mechanical properties of MgZnYLaMM alloys, *Metall. Mater. Trans. A* 43 (2012) 4383–4396. doi:10.1007/s11661-012-1239-9.
- [17] E. Oñorbe, G. Garcés, F. Dobes, P. Pérez, P. Adeva, High-temperature mechanical behavior of extruded Mg-Y-Zn alloy containing LPSO phases, *Metall. Mater. Trans. A* 44 (2013) 2869–2883. doi:10.1007/s11661-013-1628-8.
- [18] P. Pérez, J. Medina, G. Garcés, P. Adeva, Influence of Y/CeMM ratio on the microstructure and mechanical properties of Mg<sub>95</sub>Zn<sub>2</sub>(Y,CeMM)<sub>3</sub> alloys, *Intermetallics* 31 (2012) 196–201. doi:10.1016/j.intermet.2012.07.005.
- [19] X. Tan, K.H.W. Chee, K.W.J. Chan, W.O. Richard Kwok, M. Gupta, Effect of homogenization on enhancing the failure strain of high strength quaternary LPSO Mg–Y–Zn–Al alloy, *Mater. Sci. Eng. A* 644 (2015) 405–412. doi:10.1016/j.msea.2015.07.079.
- [20] J. Wang, J. Zhang, X. Zong, C. Xu, Z. You, K. Nie, Effects of Ca on the formation of LPSO phase and mechanical properties of Mg-Zn-Y-Mn alloy, *Mater. Sci. Eng. A* 648 (2015) 37–40. doi:10.1016/j.msea.2015.09.046.
- [21] P. Pérez, S. González, G. Garcés, G. Caruana, P. Adeva, High-strength extruded Mg<sub>96</sub>Ni<sub>2</sub>Y<sub>1</sub>RE<sub>1</sub> alloy exhibiting superplastic behaviour, *Mater. Sci. Eng. A* 485 (2008) 194–199. doi:10.1016/j.msea.2007.07.083.
- [22] K. Milička, P. Pérez, F. Dobeš, G. Garcés, P. Adeva, Creep of high-strength Mg-Ni-Y-RE alloys, *Mater. Sci. Eng. A* 510-511 (2009) 377–381. doi:10.1016/j.msea.2008.06.059.
- [23] P. Pérez, S. González, G. Garcés, Influence of partial replacement of cerium-rich mischmetal (CeMM) by yttrium on the crystallization and

- mechanical properties of amorphous Mg<sub>80</sub>Ni<sub>10</sub>CeMM10 alloy, *Intermetallics*. 15 (2007) 315–326. doi:10.1016/j.intermet.2006.07.008.
- [24] S. Wu, J. Zhang, Z. Zhang, C. Xu, K. Nie, X. Niu, A high strength and good ductility Mg–Y–Ni–Ti alloy with long period stacking ordered structure processed by hot rolling and aging treatment, *Mater. Sci. Eng. A*. 648 (2015) 134–139. doi:10.1016/j.msea.2015.09.057.
- [25] M. Jiang, S. Zhang, Y. Bi, H. Li, Y. Ren, G. Qin, Phase equilibria of the long-period stacking ordered phase in the Mg–Ni–Y system, *Intermetallics*. 57 (2015) 127–132. doi:10.1016/j.intermet.2014.10.014.
- [26] J.Y. Lee, D.H. Kim, H.K. Lim, D.H. Kim, Effects of Zn/Y ratio on microstructure and mechanical properties of Mg–Zn–Y alloys, *Mater. Lett.* 59 (2005) 3801–3805. doi:10.1016/j.matlet.2005.06.052.
- [27] P. Pérez, G. Garcés, P. Adeva, Microstructure and mechanical properties of a rapidly solidified Mg<sub>94.5</sub>Zn<sub>2</sub>Y<sub>1.5</sub>LaMM<sub>1.5</sub>Mn<sub>0.5</sub> alloy, *J. Alloys Compd.* 491 (2010) 192–199. doi:10.1016/j.jallcom.2009.11.012.
- [28] S. González, G. Garcés, P. Adeva, P. Pérez, Influence of processing route on microstructure and mechanical properties of two Mg–Ni–Y–RE alloys, *Mater. Character.* 64 (2012) 53–61. doi: 10.1016/j.matchar.2011.12.001.
- [29] G. Garcés, M. Rodríguez, P. Pérez, P. Adeva, Microstructural and mechanical characterisation of WE54–SiC composites, *Mater. Sci. Eng. A* 527 (2010) 6511–6517. doi:10.1016/j.msea.2010.07.026
- [30] S. Cabeza, G. Garcés, P. Pérez, P. Adeva, Microstructure and mechanical behavior of powder metallurgy Mg<sub>98.5</sub>Gd<sub>1</sub>Zn<sub>0.5</sub> alloy, *Metall. Mater. Trans. A* 45 (2014) 3222–3231, doi: 10.1007/s11661-013-2041-z.
- [31] N. Tahreen, D.F. Zhang, F.S. Pan, X.Q. Jiang, C. Li, D.Y. Li, D.L. Chen, Influence of yttrium content on phase formation and strain hardening behavior of Mg–Zn–Mn magnesium alloy, *J. Alloys Compd.* 615 (2014), 424–432. doi:10.1016/j.jallcom.2014.06.211.
- [32] H.J. Frost and M.F. Ashby, *Deformation-Mechanism Maps: The Plasticity and Creep of Metals and Ceramics*, Pergamon, Oxford, 1982.
- [33] W.J. Kim, S.W. Chung, C.S. Chung, D. Kum, Superplasticity in thin magnesium alloy sheets and deformation mechanism maps for magnesium alloys at elevated temperatures, *Acta Mater* 49 (2001) 3337–3345, doi:10.1016/S1359-6454(01)00008-8.

- [34] L. Li, X.M. Zhang, Hot compression deformation behavior and processing parameters of a cast Mg–Gd–Y–Zr alloy, *Mater. Sci. Eng. A* 528 (2011) 1396–1401. doi:10.1016/j.msea.2010.10.026
- [35] Q. Chen, X.S. Xia, B.G. Yuan, D.Y. Shu, Z. Zhao, J.C. Han, Hot workability behavior of as-cast Mg–Zn–Y–Zr alloy, *Mater. Sci. Eng. A* 593 (2014) 38–47. doi:10.1016/j.msea.2013.11.014.
- [36] N. Tahreen, D.F. Zhang, F.S. Pan, X.Q. Jiang, C. Li, D.Y. Li, D.L. Chen, Characterization of hot deformation behavior of an extruded Mg–Zn–Mn–Y alloy containing LPSO phase, *J. Alloys Compd.* 644 (2015), 814–823. *J. Alloys Compd.* 615 (2014), 424–432. doi:10.1016/j.jallcom.2015.04.144.
- [37] C. Sanchez, G. Nussbaum, P. Azavant, H. Octor, Elevated temperature behaviour of rapidly solidified magnesium alloys containing rare earths, *Mater. Sci. Eng. A* 221 (1996) 48–57. doi:10.1016/S0921-5093(96)10469-X
- [38] H. Zhang, S. Wang, First-principles study on the phase stability of Mg–La and Mg–Nd binary alloys, *Acta Metall. Sin.* 48 (2013) 889–894. doi:10.3724/SP.J.1037.2012.00089.
- [39] E. Oñorbe, G. Garcés, P. Pérez, P. Adeva, Effect of the LPSO volume fraction on the microstructure and mechanical properties of Mg–Y<sub>2</sub>X–ZnX alloys, *J. Mater. Sci.* 47 (2011) 1085–1093. doi:10.1007/s10853-011-5899-4.
- [40] E. Oñorbe, G. Garcés, P. Pérez, S. Cabezas, M. Klaus, C. Genzel, E. Frutos, P. Adeva, The evolution of internal strain in Mg–Y–Zn alloys with a long period stacking ordered structure, *Scr. Mater.* 65 (2011) 719–722. doi:10.1016/j.scriptamat.2011.07.017.
- [41] M. Tane, Y. Nagai, H. Kimizuka, K. Hagihara, Y. Kawamura, Elastic properties of an Mg–Zn–Y alloy single crystal with a long-period stacking-ordered structure, *Acta Mater.* 61 (2013) 6338–6351. doi:10.1016/j.actamat.2013.06.041.
- [42] P. Greenfield, W. Vickers, The creep properties of a compacted magnesium alloy powder, *J. Nuclear Mater.* 22 (1967) 77–87.
- [43] K. Milička, J. Čadek, P. Ryš, High temperature creep mechanisms in magnesium, *Acta Metall.* 18 (1970) 1071–1082. doi:10.1016/0001-6160(70)90005-2.

- [44] P. Pérez, G. Garcés, P. Adeva, Influence of texture on the mechanical properties of commercially pure magnesium prepared by powder metallurgy, *J. Mater. Sci.* 42 (2007) 3969–3976. doi:10.1007/s10853-006-1301-3.
- [45] K. Milička, F. Dobeš, P. Pérez, G. Garcés, P. Adeva, Anisotropy of creep resistance in extruded magnesium, *Scr. Mater.* 61 (2009) 1109–1112. doi:10.1016/j.scriptamat.2009.08.033.
- [46] B.Q. Han, D.C. Dunand, Creep of magnesium strengthened with high volume fractions of yttria dispersoids, *Mater. Sci. Eng. A.* 300 (2001) 235–244. doi:10.1016/S0921-5093(00)01781-0.
- [47] H. Ferkel, B.L. Mordike, Magnesium strengthened by SiC nanoparticles, *Mater. Sci. Eng. A.* 298 (2001) 193–199. doi:10.1016/S0921-5093(00)01283-1.
- [48] P. Pérez, G. Garcés, P. Adeva, Influence of titanium volume fraction on the mechanical properties of Mg-Ti composites, *Int. J. Mater. Res.* 100 (2009) 366–369. doi: 10.3139/146.110023.
- [49] K.-T. Park, F.A. Mohamed, Creep strengthening in a discontinuous SiC-Al composite, *Metall. Mater. Trans. A* 26 (1995) 3119–3129. doi: 10.1007/BF02669441.
- [50] Y. Li, T.G. Langdon, A comparison of the creep properties of an Al-6092 composite and the unreinforced matrix alloy, *Metall. Mater. Trans. A* 29 (1998) 2523–2531. doi:10.1007/s11661-998-0224-9.
- [51] Y. Li, T.G. Langdon, Unified interpretation of threshold stresses in the creep and high strain rate superplasticity of metal matrix composites, *Acta Mater.* 47 (1999) 3395–3403. doi:10.1016/S1359-6454(99)00219-0.
- [52] Z.Y. Ma, R.S. Mishra, S.C. Tjong, High-temperature creep behavior of TiC particulate reinforced Ti–6Al–4V alloy composite, *Acta Mater.* 50 (2002) 4293–4302. doi:10.1016/S1359-6454(02)00261-6.
- [53] S.E. Ion, F.J. Humphreys, S.H. White, Dynamic recrystallisation and the development of microstructure during the high temperature deformation of magnesium, *Acta Metall.* 30 (1982) 1909–1919. doi:10.1016/0001-6160(82)90031-1.
- [54] K. Hagihara, A. Kinoshita, Y. Sugino, M. Yamasaki, Y. Kawamura, H.Y. Yasuda, Y. Umakoshi, Plastic deformation behavior of Mg<sub>97</sub>Zn<sub>1</sub>Y<sub>2</sub>

- extruded alloys, *Trans. Nonferrous Met. Soc. China (English Ed.* 20 (2010) 1259–1268. doi:10.1016/S1003-6326(09)60288-0.
- [55] G. Garcés, M.A. Muñoz-Morris, D.G. Morris, J.A. Jiménez, P. Pérez, P. Adeva, The role of extrusion texture on strength and its anisotropy in a Mg-base alloy composed of the Long-Period-Structural-Order phase, *Intermetallics*. 55 (2014) 167–176. doi:10.1016/j.intermet.2014.07.015.
- [56] P. Pérez, M. Eddahbi, S. González, G. Garcés, P. Adeva, Refinement of the microstructure during superplastic deformation of extruded Mg<sub>94</sub>Ni<sub>3</sub>Y<sub>1.5</sub>CeMM<sub>1.5</sub> alloy, *Scr. Mater.* 64 (2011) 33–36. doi:10.1016/j.scriptamat.2010.08.059.
- [57] H. Watanabe, M. Fukusumi, H. Somekawa, T. Mukai, Texture and mechanical properties of superplastically deformed magnesium alloy rod, *Mater. Sci. Eng. A*. 527 (2010) 6350–6358. doi:10.1016/j.msea.2010.06.053.
- [58] W.J. Kim, H.W. Lee, S.J. Yoo, Y.B. Park, Texture and mechanical properties of ultrafine-grained Mg–3Al–1Zn alloy sheets prepared by high-ratio differential speed rolling, *Mater. Sci. Eng. A*. 528 (2011) 874–879. doi:10.1016/j.msea.2010.09.007.



**Table Captions**

Table 1. Values of  $n$  for all MgNi<sub>2</sub> and MgNi<sub>3</sub> alloys depending on the temperature and strain rate.

Accepted manuscript

**Figure Captions**

- Fig. 1. Backscattered SEM images of the microstructures along the extrusion direction of the alloys extruded at 400°C. (a) CP-MgNi<sub>2</sub>, (b) PM-MgNi<sub>2</sub>, (c) CP-MgNi<sub>3</sub>, (d) PM-MgNi<sub>3</sub>.
- Fig. 2. True stress - true strain curves for all materials at different temperatures. (a) 100°C, (b) 200°C, (c) 250°C, (d) 300°C, (e) 350°C, (f) 400°C.
- Fig. 3. Evolution of the mechanical properties for all alloys in the 100-400°C temperature range. (a) Yield stress, (b) maximum strength, (c) elongation to failure.
- Fig. 4. Strain rate–true stress plot at different temperatures for CP and PM alloys. (a) 100°C, (b) 200°C, (c) 300°C, (d) 350°C, (e) 400°C.
- Fig. 5. Microstructure of the longitudinal section for the CP-MgNi<sub>2</sub> alloy deformed to failure at 200°C. (a) Outside the necked region, (b) inside the necked region.
- Fig. 6. Microstructural features observed in the longitudinal section of the PM-MgNi<sub>2</sub> alloy deformed to failure at 200°C: (a) Voids close to the fracture surface, (b) absence of cracking in second phases outside the necked region, (c) numerous cracked second phases near the fracture surface. White arrows mark voids while red arrows show fragmented particles.
- Fig. 7. Grain structure along the longitudinal section of the PM-MgNi<sub>2</sub> alloy deformed to failure at 200°C: (a) Region close to the fracture surface, (b) within the necked region, (c) outside the necked region, (d) outside the gauge length in the head of the sample.
- Fig. 8. Microstructure along the longitudinal section of the samples tested at 250°C. (a) CP-MgNi<sub>3</sub> sample deformed 8 %, (b) region close to fracture of CP-MgNi<sub>2</sub> sample, (c) within the necked region in CP-MgNi<sub>2</sub> sample deformed to failure, (d) outside necked region in CP-MgNi<sub>2</sub> sample deformed to failure, (e) head of the CP-MgNi<sub>2</sub> sample deformed to failure, (f) within the necked region in CP-MgNi<sub>3</sub> sample deformed to failure. Insets show the grain structure of the magnesium matrix revealed by chemical etching.

Fig. 9. Regions close to the fracture surface in the samples tested at 250°C. (a) PM-MgNi<sub>2</sub>, (b) PM-MgNi<sub>3</sub> alloy. Red arrows illustrate some examples of cavities.

Fig. 10. Microstructure along the longitudinal section of the samples deformed to failure at 250°C. (a) PM-MgNi<sub>2</sub> (gauge length), (b) PM-MgNi<sub>2</sub> (head), (c) PM-MgNi<sub>3</sub> (gauge length), (d) PM-MgNi<sub>3</sub> (head).

Fig. 11. Fracture of second phases during plastic deformation of CP-MgNi<sub>3</sub> alloy. (a) Sample deformed 8 % at 300°C, (b) sample deformed 40 % at 350°C.

Fig. 12. Longitudinal sections showing the redistribution of second phases during superplastic deformation: (a) CP-MgNi<sub>2</sub> alloy deformed to failure at 300°C (b) CP-MgNi<sub>2</sub> alloy deformed 250 % at 400°C, (c) CP-MgNi<sub>3</sub> alloy deformed to failure at 300°C, (d) CP-MgNi<sub>3</sub> alloy deformed to failure at 400°C. The insets reveal the grain structure in the deformed regions.

Fig. 13. Cavities developed in regions near the fracture surface in PM alloys deformed at 350°C. (a) PM-MgNi<sub>2</sub> alloy, (b) PM-MgNi<sub>3</sub> alloy.

Fig. 14. Microstructure of MgNi<sub>3</sub> samples tensile tested at 300°C. (a) 30 % of elongation, (b) 90 % of elongation, (c) 150 % of elongation, (d) up to failure.

Table 1. Values of the stress exponent  $n$  between 100 and 400°C for all MgNi<sub>2</sub> and MgNi<sub>3</sub> alloys.

<b>T (°C)</b>	<b>CP-MgNi<sub>2</sub></b>		<b>PM-MgNi<sub>2</sub></b>		<b>CP-MgNi<sub>3</sub></b>		<b>PM-MgNi<sub>3</sub></b>	
	<b><math>n</math></b>	<b><math>\dot{\epsilon}</math> (<math>s^{-1}</math>)</b>	<b><math>n</math></b>	<b><math>\dot{\epsilon}</math> (<math>s^{-1}</math>)</b>	<b><math>n</math></b>	<b><math>\dot{\epsilon}</math> (<math>s^{-1}</math>)</b>	<b><math>n</math></b>	<b><math>\dot{\epsilon}</math> (<math>s^{-1}</math>)</b>
100	22	$10^{-4}$ - $10^{-3}$	35	$10^{-5}$ - $10^{-2}$				
200	46	$10^{-4}$ - $3 \times 10^{-2}$	29	$10^{-5}$ - $10^{-2}$	18	$10^{-5}$ - $10^{-2}$	16	$10^{-4}$ - $3 \times 10^{-2}$
300	7	$> 3 \times 10^{-3}$	$> 5$	$> 3 \times 10^{-3}$	$> 5$	$> 10^{-3}$	$> 8$	$> 3 \times 10^{-2}$
	2	$< 3 \times 10^{-4}$	2.5	$3 \times 10^{-4}$ - $3 \times 10^{-3}$	2.5	$< 10^{-3}$	3	$10^{-4}$ - $10^{-2}$
350			$> 6$	$< 3 \times 10^{-5}$			$> 5$	$< 10^{-4}$
	2	$3 \times 10^{-5}$ - $3 \times 10^{-3}$	2	$> 3 \times 10^{-3}$	2.5	$10^{-5}$ - $10^{-2}$	2	$> 3 \times 10^{-2}$
400			8	$< 10^{-4}$			4	$< 3 \times 10^{-3}$
	2	$10^{-4}$ - $3 \times 10^{-2}$			2	$3 \times 10^{-3}$ - $3 \times 10^{-2}$	2	$> 3 \times 10^{-2}$
					4.5	$3 \times 10^{-5}$ - $3 \times 10^{-4}$	7	$< 10^{-3}$

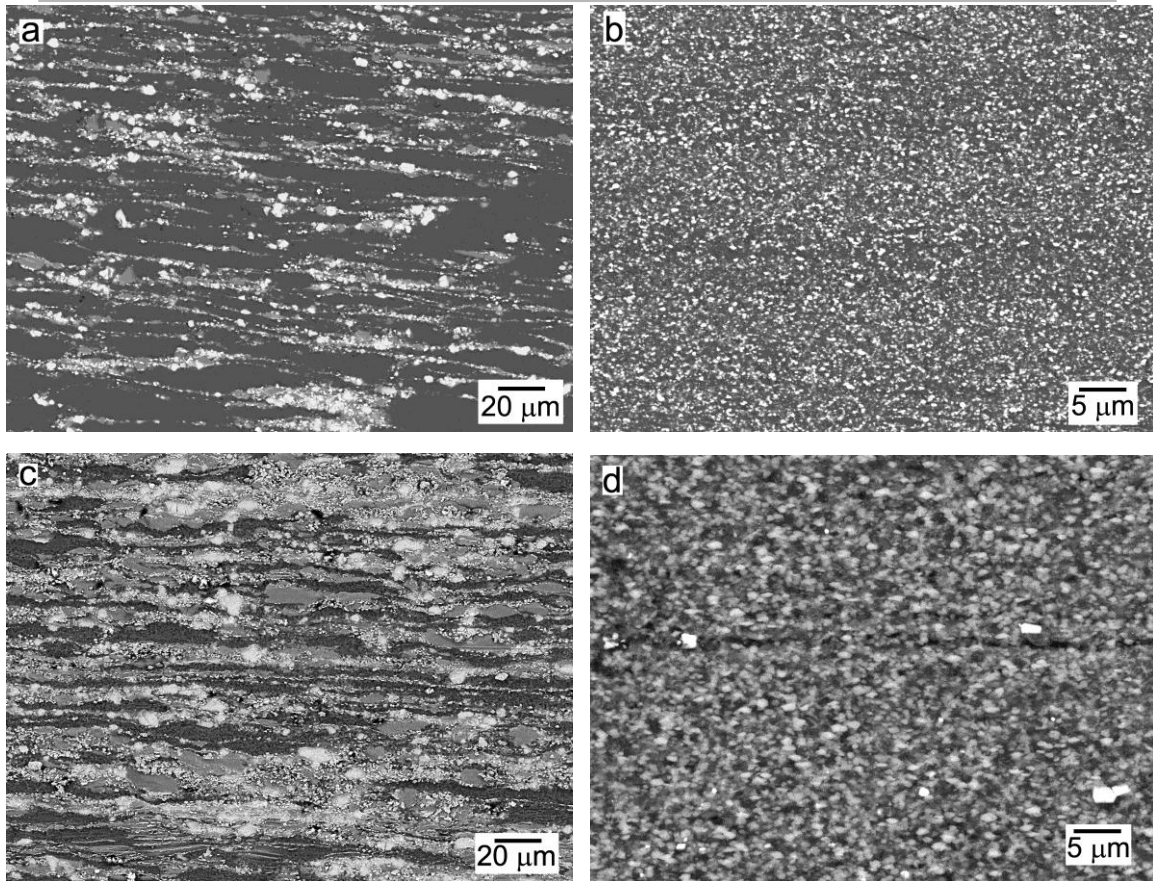


Fig. 1. Backscattered SEM images of the microstructures along the extrusion direction of the alloys extruded at 400°C. (a) CP-MgNi<sub>2</sub>, (b) PM-MgNi<sub>2</sub>, (c) CP-MgNi<sub>3</sub>, (d) PM-MgNi<sub>3</sub>.

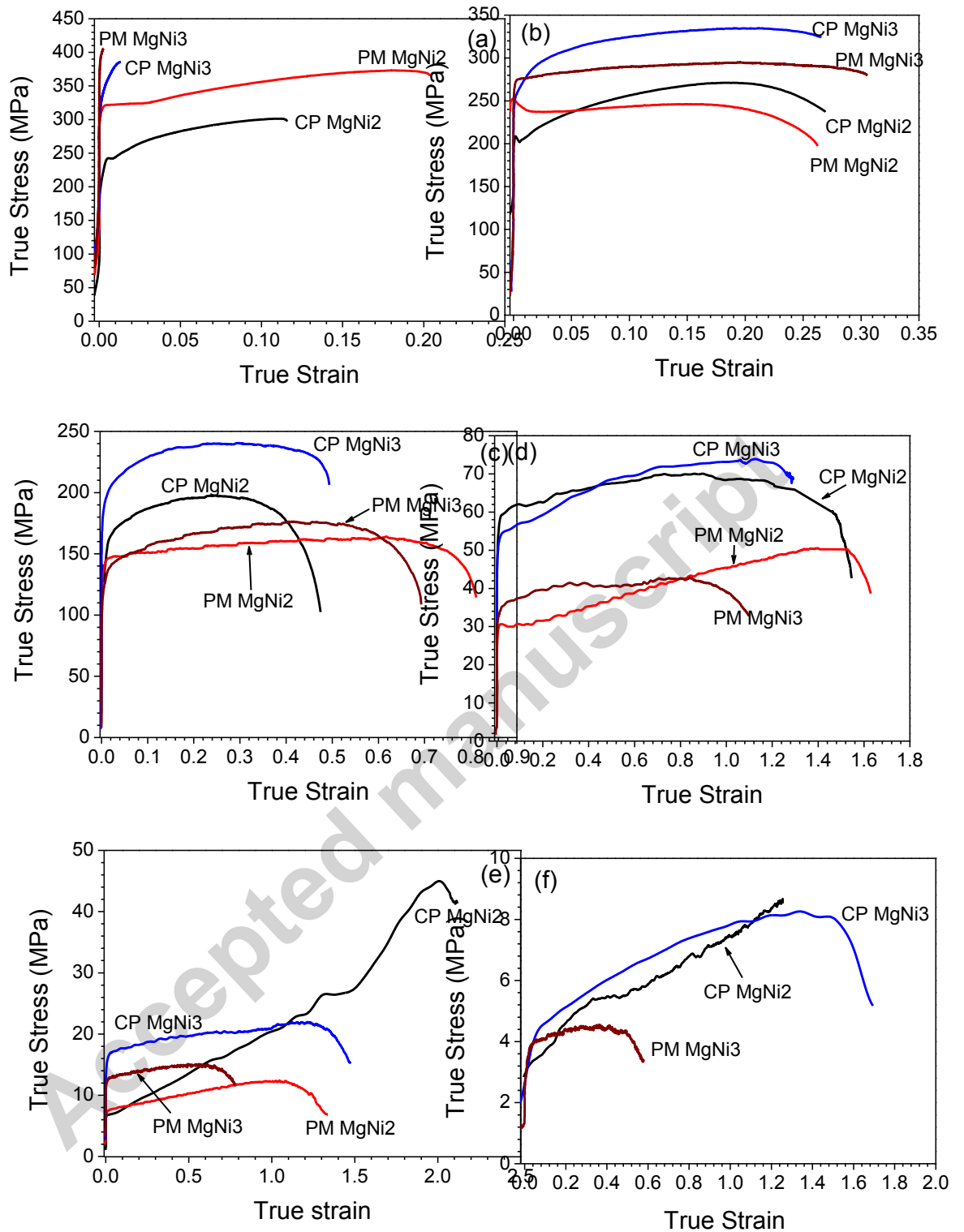


Fig. 2. True stress - true strain curves for all materials at different temperatures. (a) 100°C, (b) 200°C, (c) 250°C, (d) 300°C, (e) 350°C, (f) 400°C.

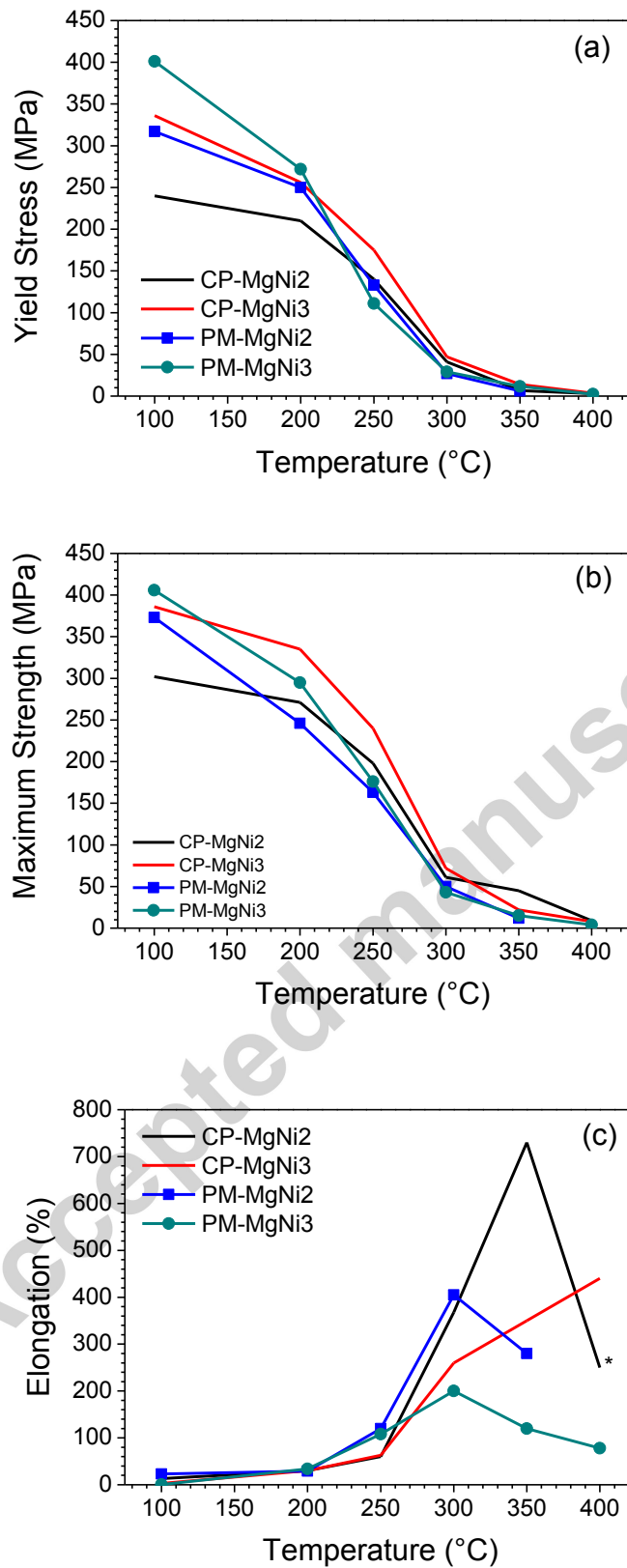


Fig. 3. Evolution of the mechanical properties for all alloys in the 100-400°C temperature range. (a) Yield stress, (b) maximum strength, (c) elongation to failure.

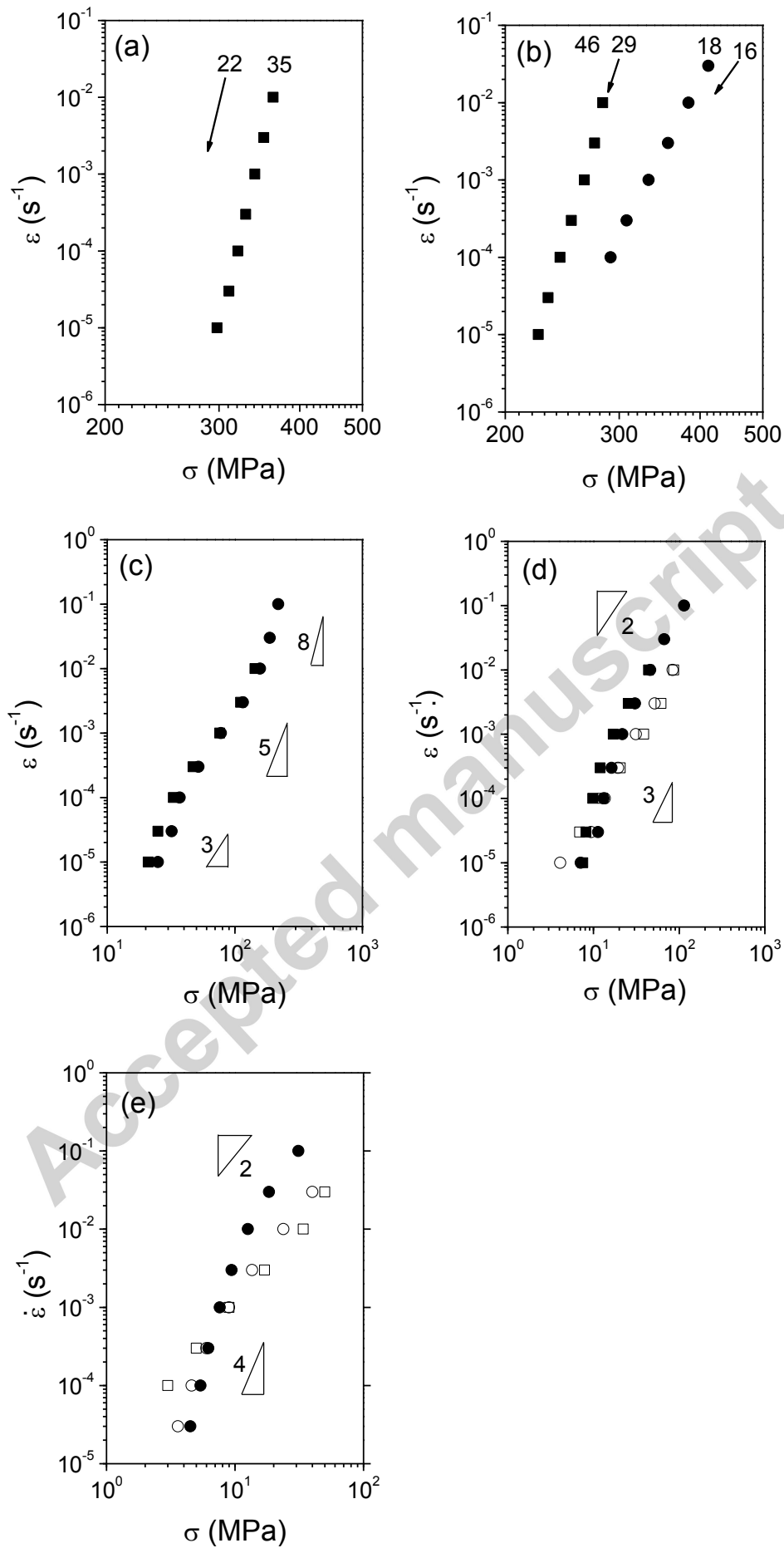


Fig. 4. Strain rate–true stress plot at different temperatures for CP and PM alloys. (a) 100°C, (b) 200°C, (c) 300°C, (d) 350°C, (e) 400°C. (□ CP-MgNi<sub>2</sub>, ■ PM-MgNi<sub>2</sub>, ○ CP-MgNi<sub>3</sub>, ● PM-MgNi<sub>3</sub>)

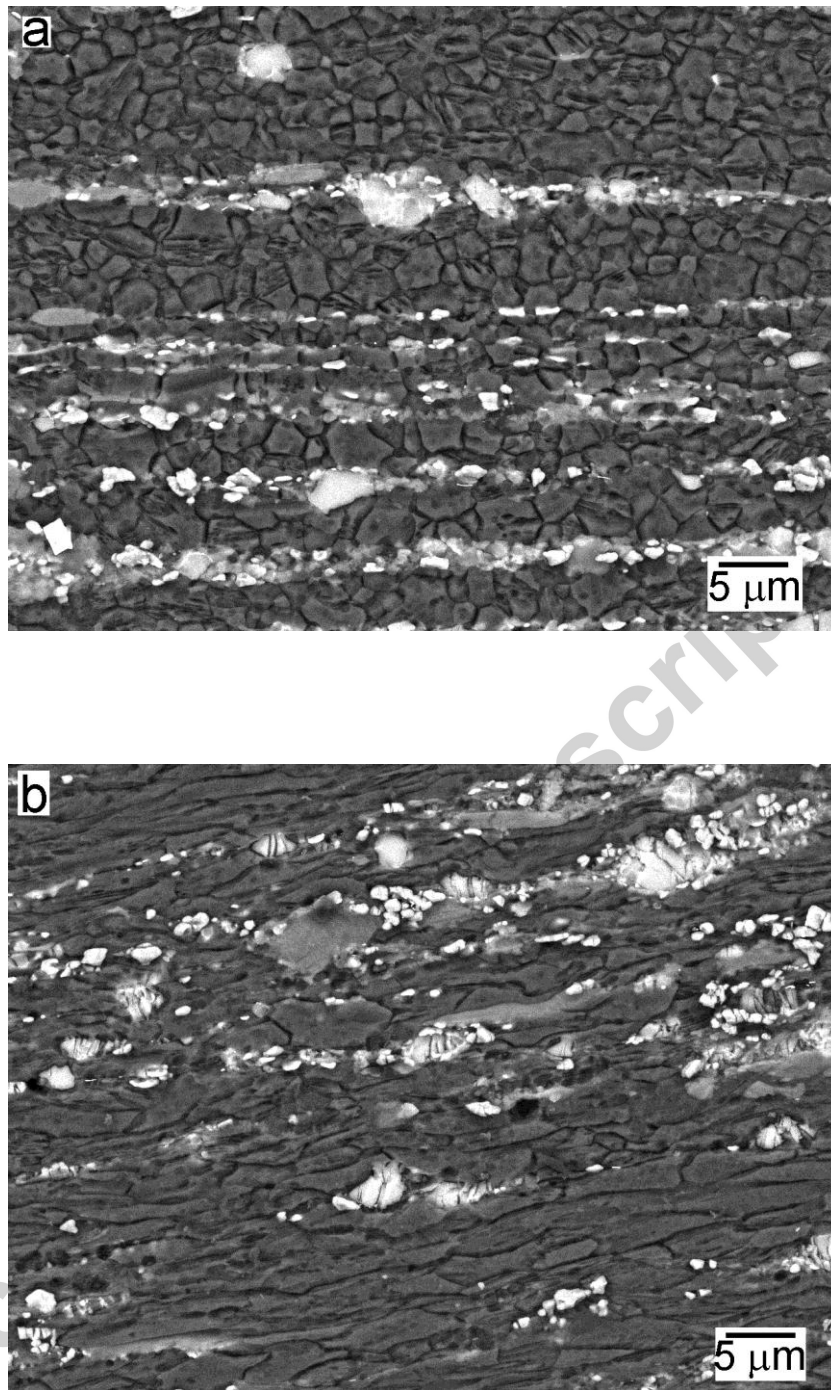


Fig. 5. Microstructure of the longitudinal section for the CP-MgNi<sub>2</sub> alloy deformed to failure at 200°C. (a) Outside the necked region, (b) inside the necked region.



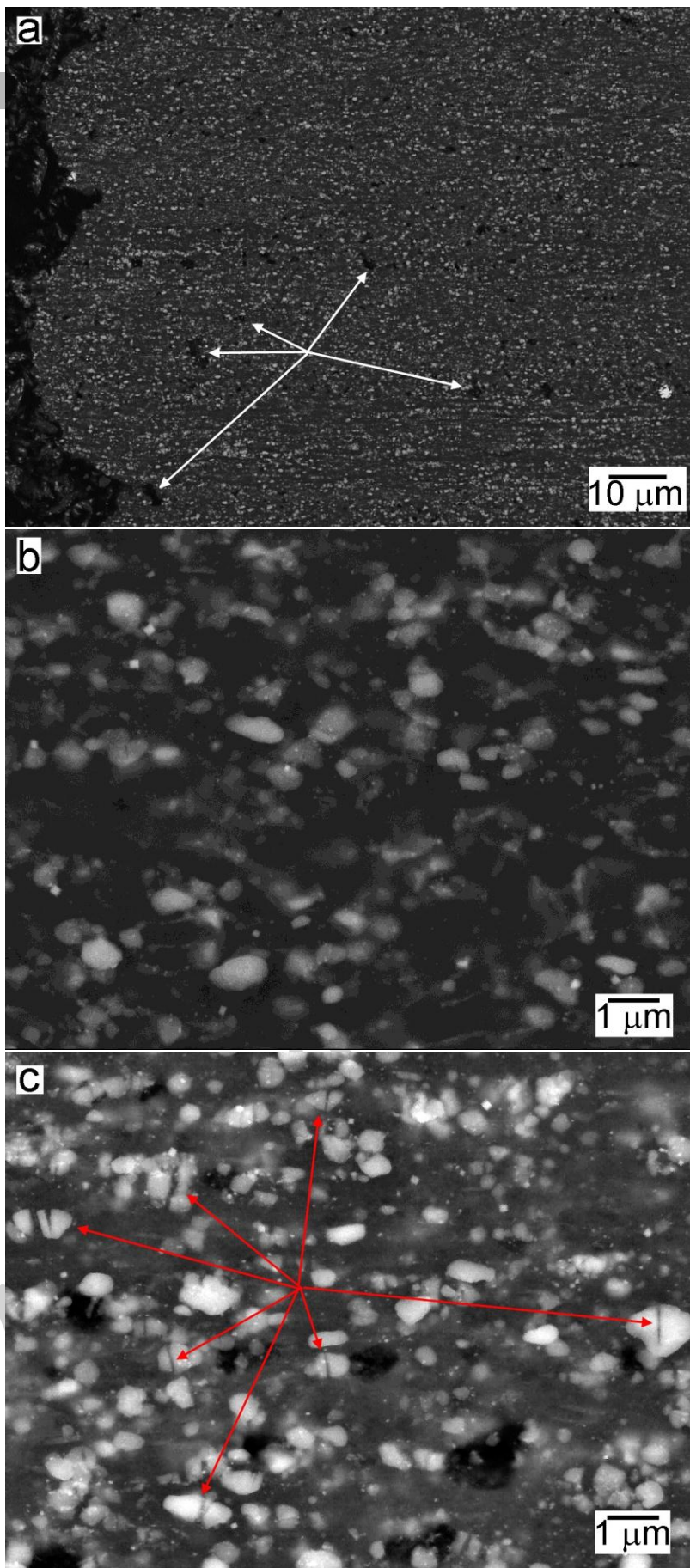


Fig. 6. Microstructural features observed in the longitudinal section of the PM-MgNi<sub>2</sub> alloy deformed to failure at 200°C: (a) Voids close to the fracture surface, (b) absence of cracking in second phases outside the necked region, (c) numerous cracked second phases near the fracture surface. White arrows mark voids while red arrows show fragmented particles.

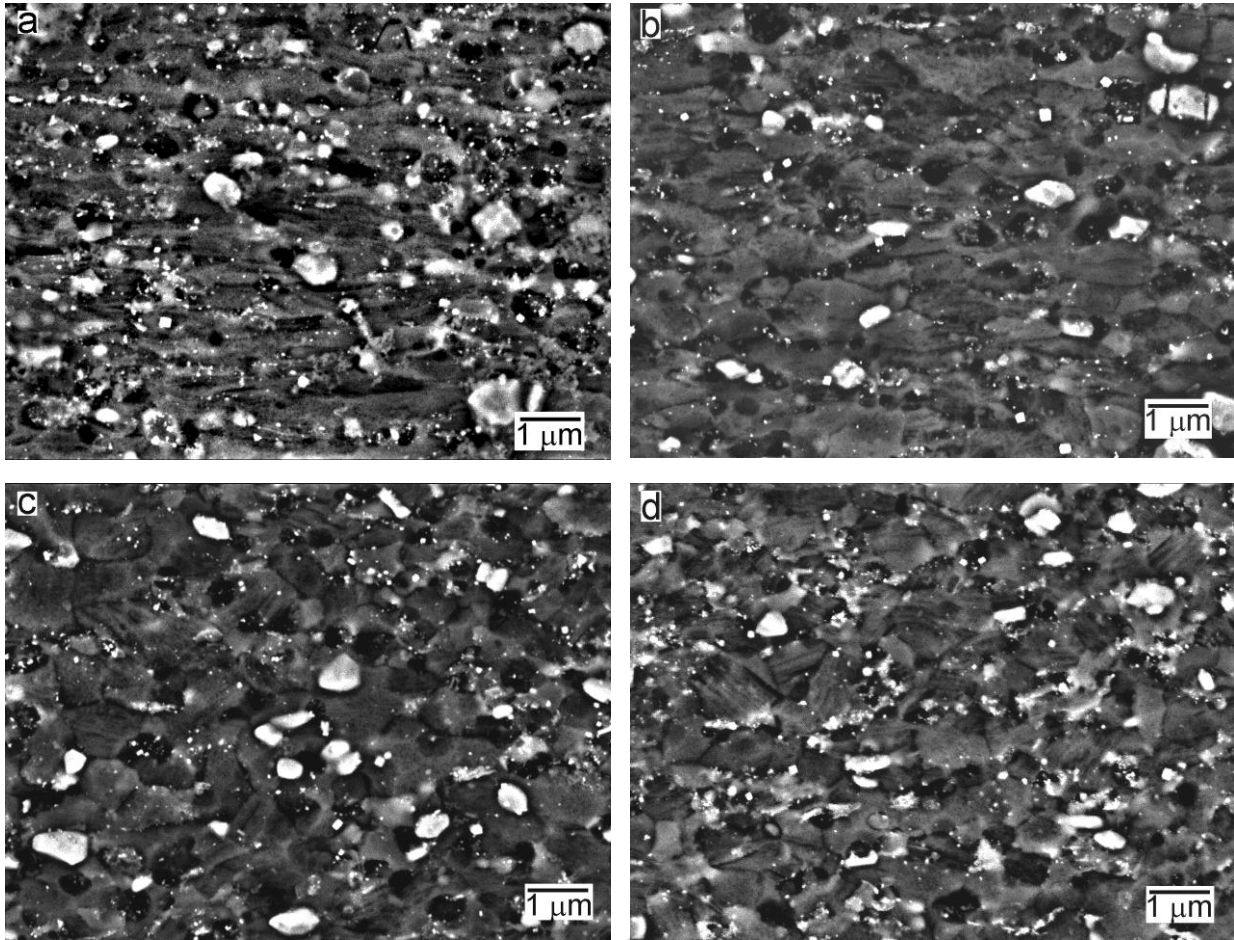


Fig. 7. Grain structure along the longitudinal section of the PM-MgNi<sub>2</sub> alloy deformed to failure at 200°C: (a) Region close to the fracture surface, (b) within the necked region, (c) outside the necked region, (d) outside the gauge length in the head of the sample.

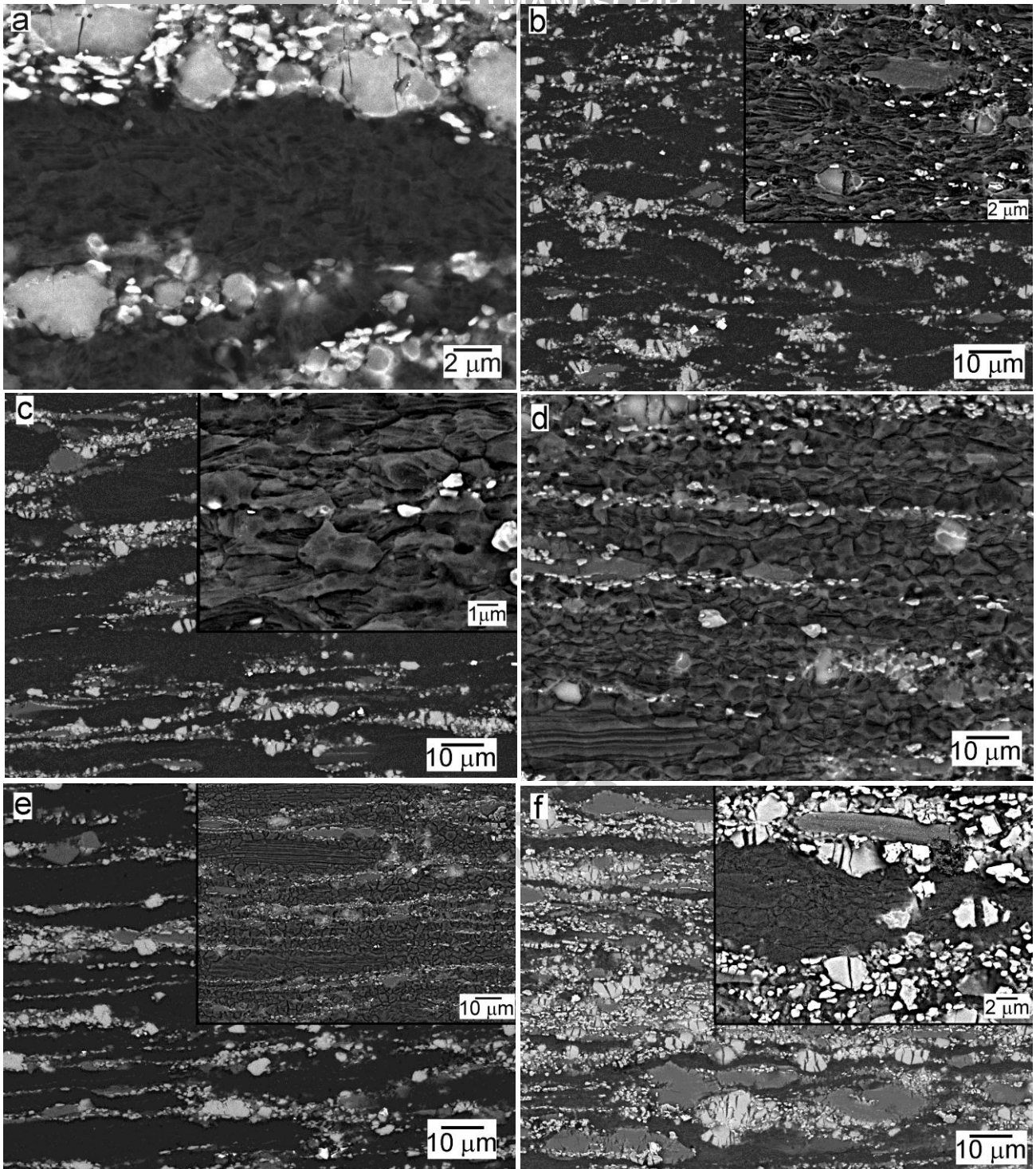


Fig. 8. Microstructure along the longitudinal section of the samples tested at 250°C. (a) CP-MgNi3 sample deformed 8 %, (b) region close to fracture of CP-MgNi2 sample, (c) within the necked region in CP-MgNi2 sample deformed to failure, (d) outside necked region in CP-MgNi2 sample deformed to failure, (e) head of the CP-MgNi2 sample deformed to failure, (f) within the necked region in CP-MgNi3 sample deformed to failure. Insets show the grain structure of the magnesium matrix revealed by chemical etching.

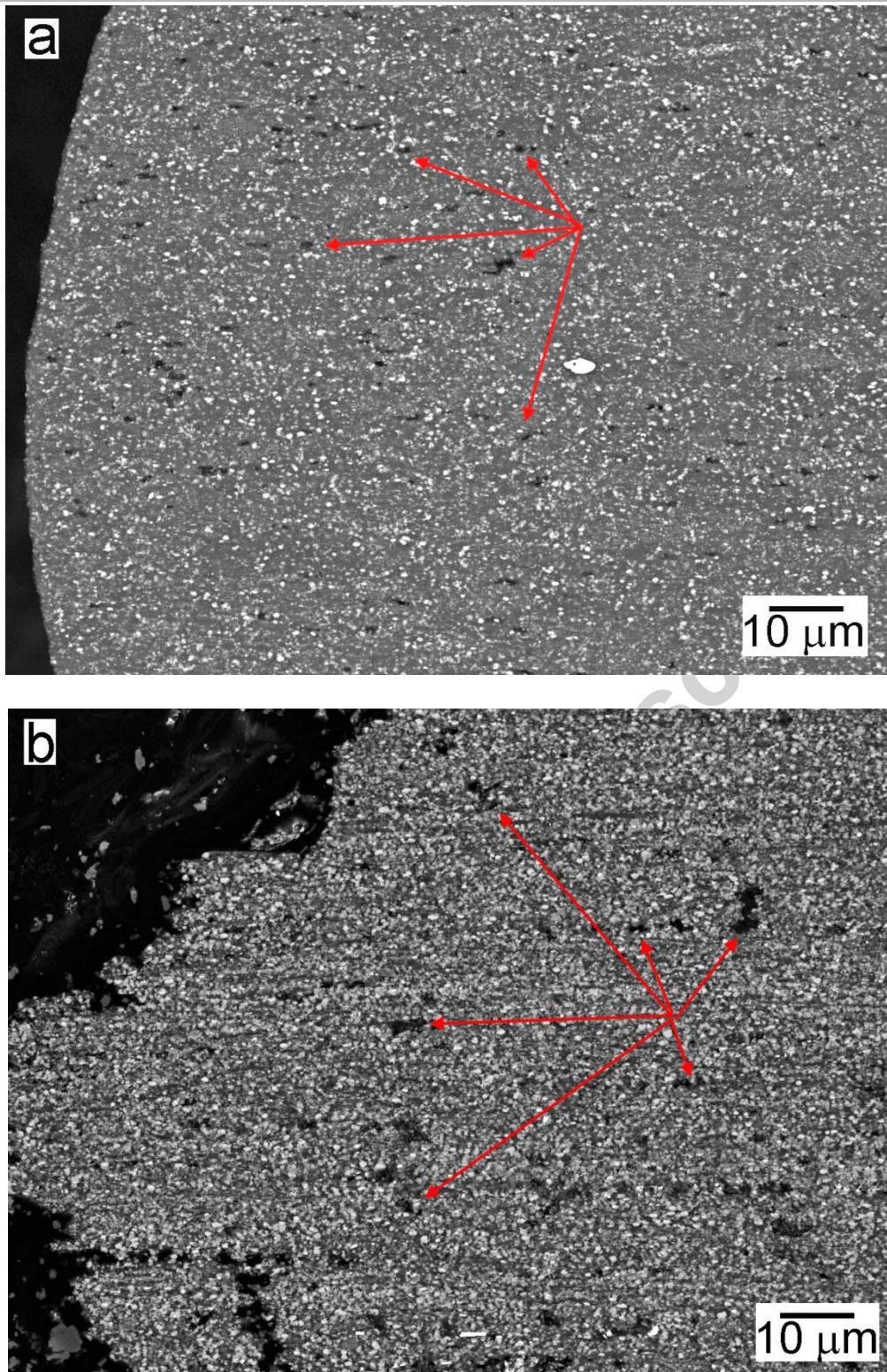


Fig. 9. Regions close to the fracture surface in the samples tested at 250°C. (a) PM-MgNi<sub>2</sub>, (b) PM-MgNi<sub>3</sub> alloy. Red arrows illustrate some examples of cavities.

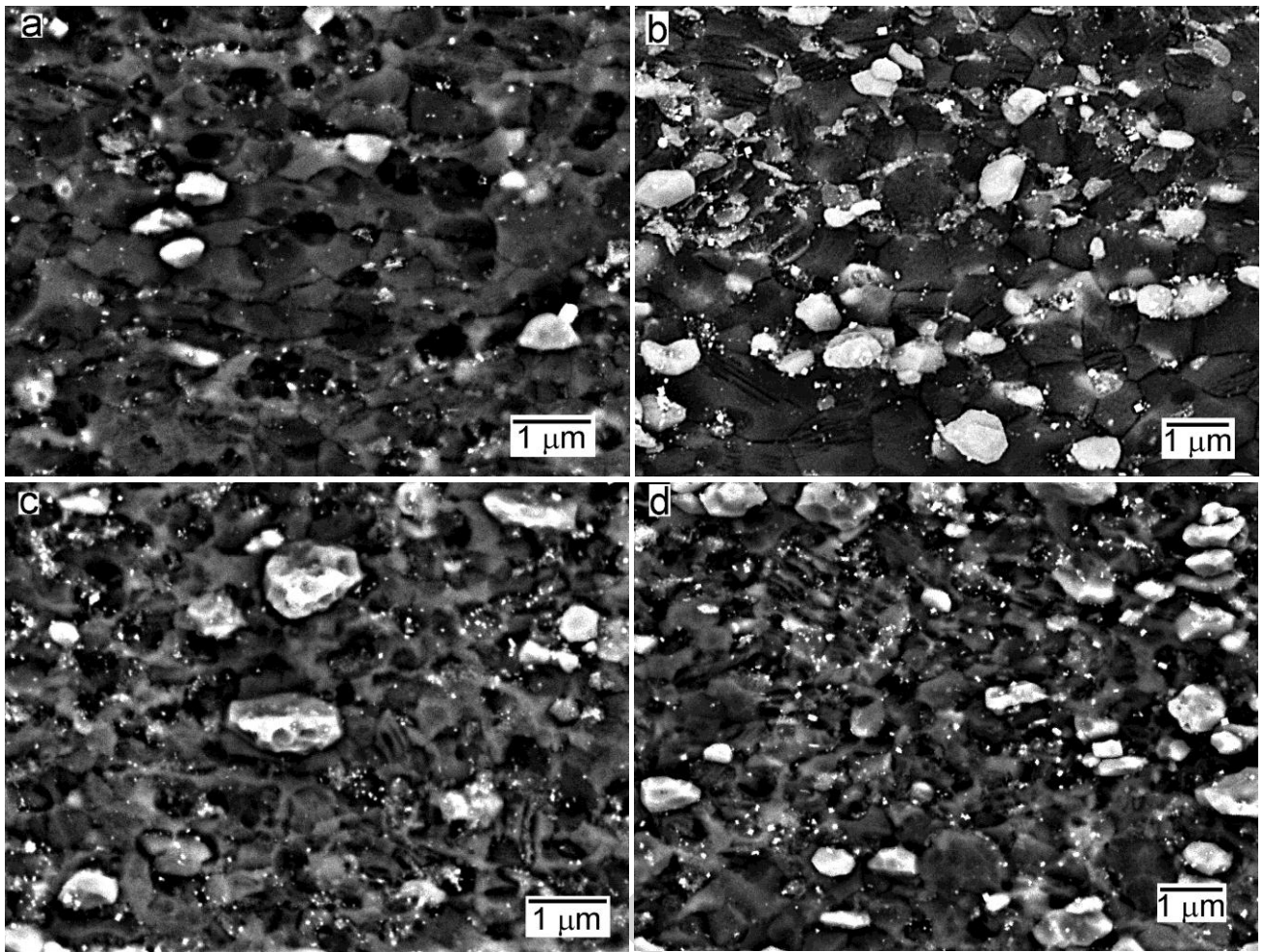


Fig. 10. Microstructure along the longitudinal section of the samples deformed to failure at 250°C. (a) PM-MgNi2 (gauge length), (b) PM-MgNi2 (head), (c) PM-MgNi3 (gauge length), (d) PM-MgNi3 (head).

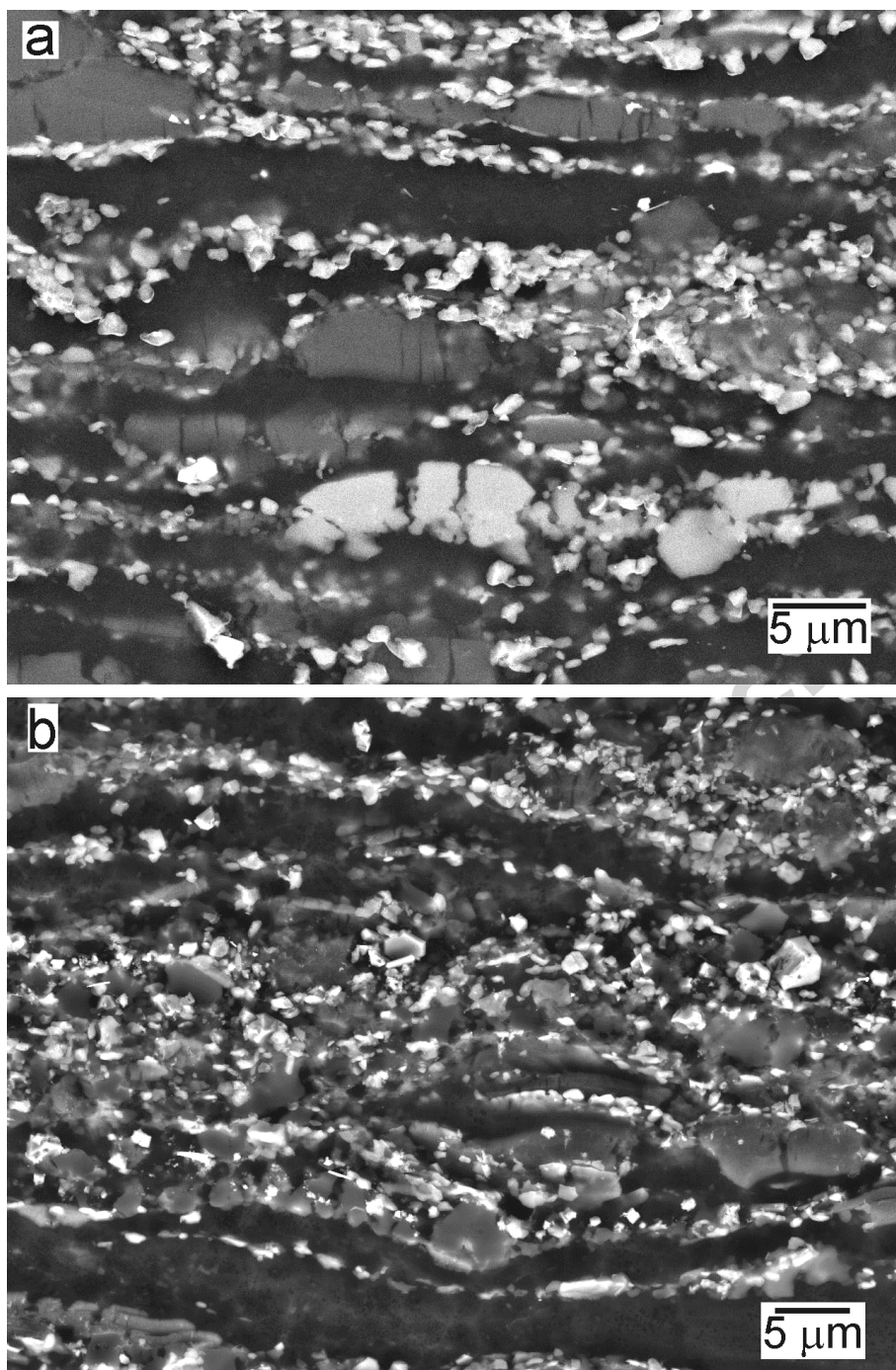


Fig. 11. Fracture of second phases during plastic deformation of CP-MgNi<sub>3</sub> alloy.  
(a) Sample deformed 8 % at 300°C, (b) sample deformed 40 % at 350°C.

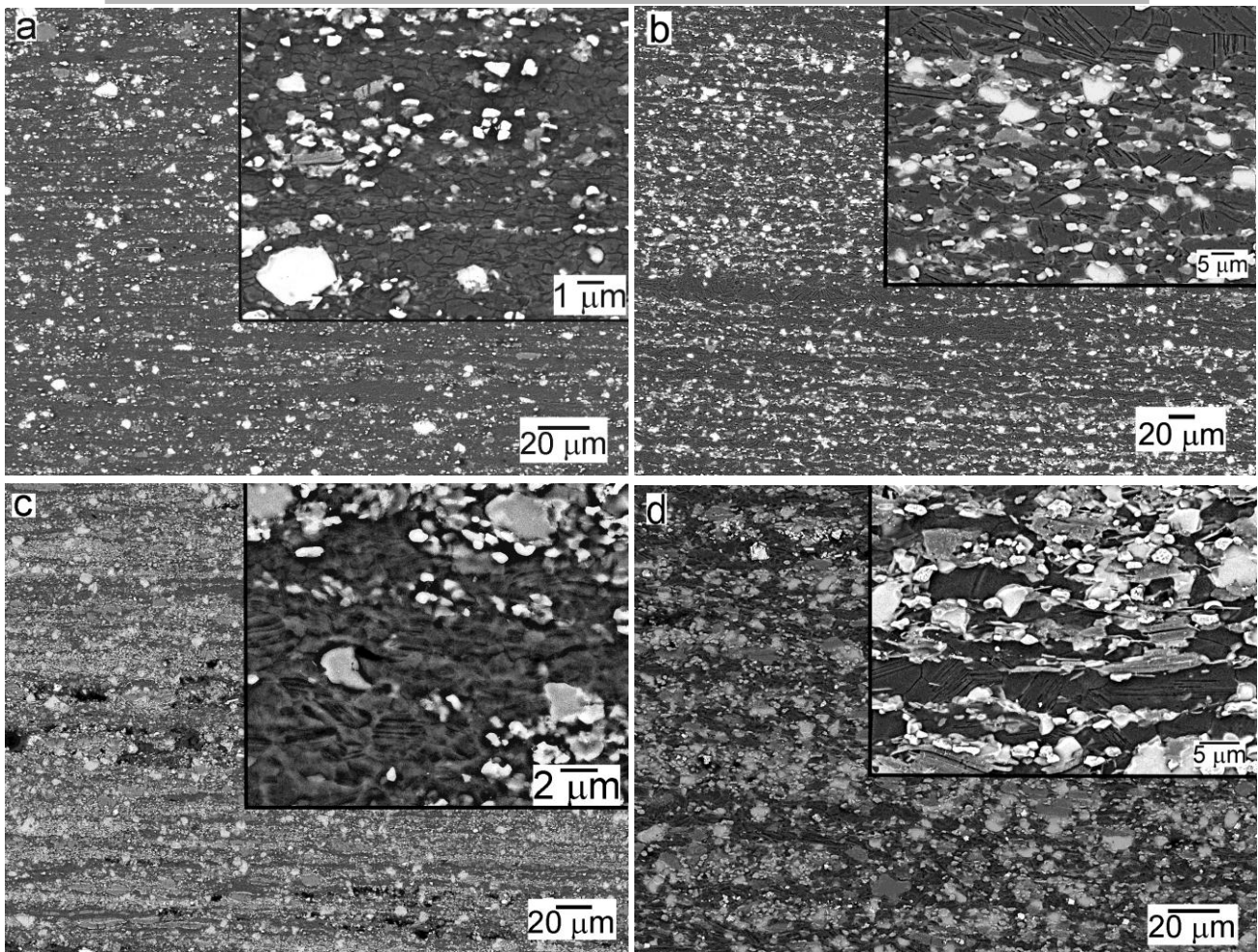


Fig. 12. Longitudinal sections showing the redistribution of second phases during superplastic deformation: (a) CP-MgNi<sub>2</sub> alloy deformed to failure at 300°C (b) CP-MgNi<sub>2</sub> alloy deformed 250 % at 400°C, (c) CP-MgNi<sub>3</sub> alloy deformed to failure at 300°C, (d) CP-MgNi<sub>3</sub> alloy deformed to failure at 400°C. The insets reveal the grain structure in the deformed regions.

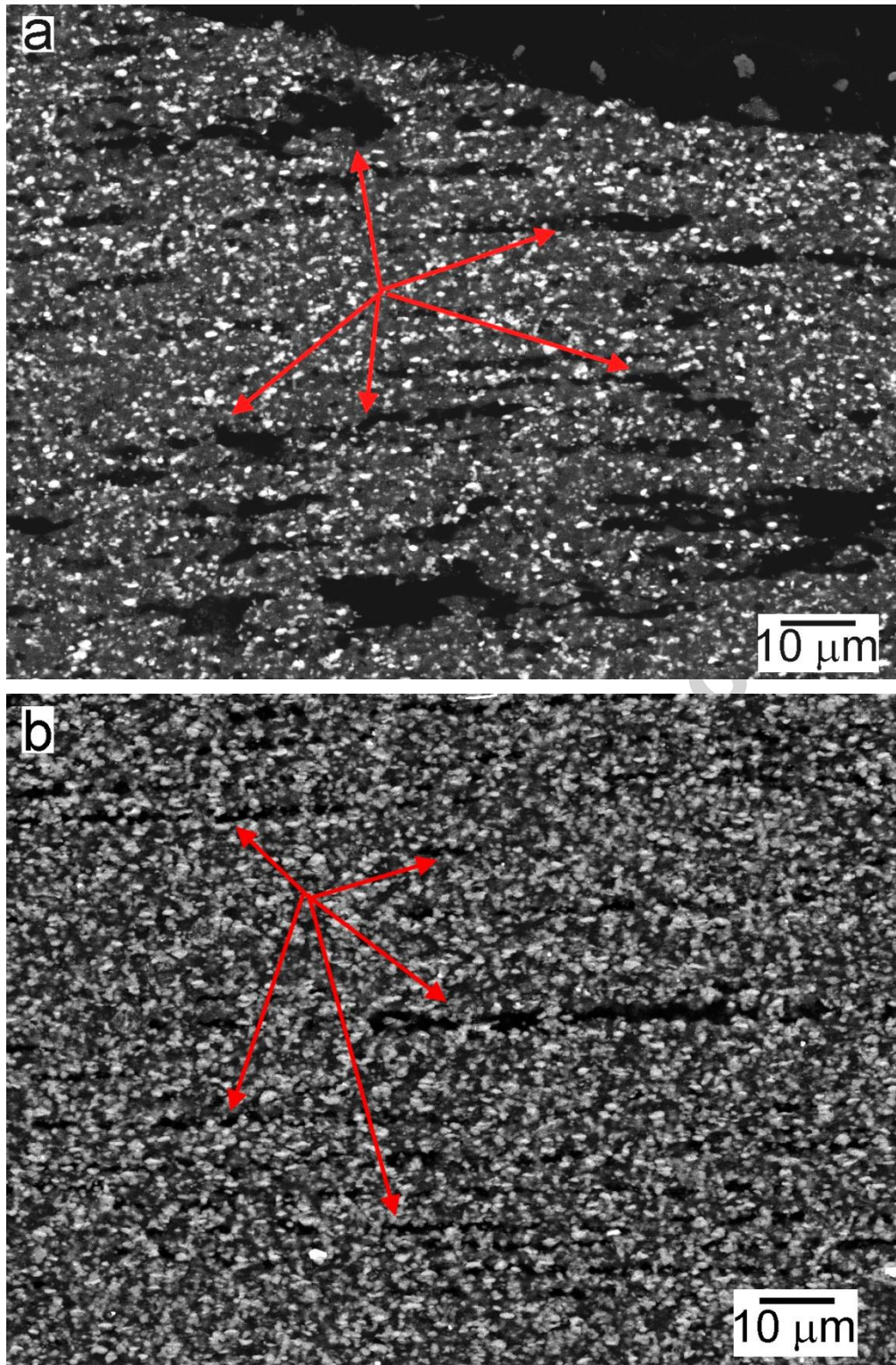


Fig. 13. Cavities developed in regions near the fracture surface in PM alloys deformed at 350°C. (a) PM-MgNi<sub>2</sub> alloy, (b) PM-MgNi<sub>3</sub> alloy.



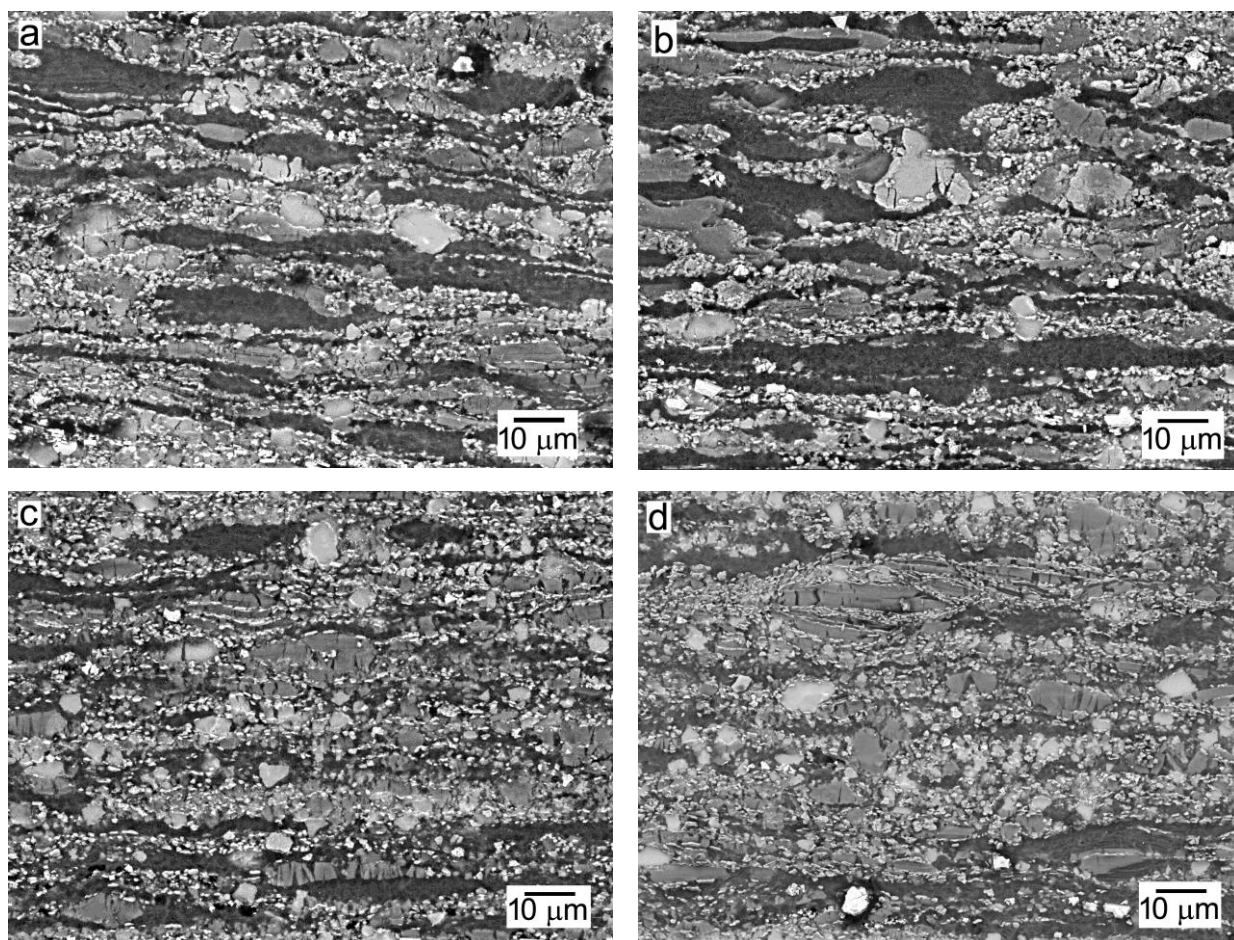


Fig. 14. Microstructure of MgNi<sub>3</sub> samples tensile tested at 300°C. (a) 30 % of elongation, (b) 90 % of elongation, (c) 150 % of elongation, (d) up to failure.